Astronomy & Astrophysics

An extensively validated C/H/O/N chemical network for hot exoplanet disequilibrium chemistry

R. Veillet[1] , O. Venot[1], B. Sirjean[2], R. Bounaceur[2], P.-A. Glaude[2], A. Al-Refaie[3], and E. Hébrard[4]

[1] Université Paris Cité and Univ. Paris-Est Créteil, CNRS, LISA, 75013 Paris, France
  e-mail: romeo.veillet@lisa.ipsl.fr
[2] Université de Lorraine, CNRS, LRGP, 54000 Nancy, France
[3] Department of Physics and Astronomy, University College London, Gower Street, London WC1E 6BT, UK
[4] Astrophysics Group, University of Exeter, Exeter EX4 4QL, UK

ABSTRACT

Context. The reliability of one-dimensional disequilibrium chemistry models in hot exoplanet atmospheres depends on the chemical network used. To develop robust networks, we can rely on combustion studies that provide C/H/O/N chemical networks validated by vast amount of experimental data generated by the extensive research that has been done on hydrocarbon combustion and NO_x formation in the last decades.

Aims. We aimed to build a new and updated C_0–C_2 chemical network to study the C/H/O/N disequilibrium chemistry of warm and hot exoplanet atmospheres that relies on extensively validated and recent state-of-the-art combustion networks. The reliability range of this network was aimed for conditions between 500–2500 K and 100–10^{-6} bar, with cautious extrapolation at lower temperature values.

Methods. We compared the predictions of seven networks over a large set of experiments, covering a wide range of conditions (pressures, temperatures, and initial compositions). To examine the consequences of this new chemical network on exoplanets atmospheric studies, we generated abundances profiles for GJ 436 b, GJ 1214 b, HD 189733 b, and HD 209458 b, using the 1D kinetic model FRECKLL and calculated the corresponding transmission spectra using TauREx 3.1. These spectra and abundance profiles have been compared with results obtained with our previous chemical network.

Results. Our new kinetic network is composed of 145 species and 1313 reactions mostly reversible. This network proves to be more accurate than our previous one for the tested experimental conditions. The nitrogen chemistry update is found to be very impactful on the abundance profiles, particularly for HCN, with differences up to four orders of magnitude. The CO_2 profiles are also significantly affected, with important repercussions on the transmission spectrum of GJ 436 b.

Conclusions. These effects highlight the importance of using extensively validated chemical networks to gain confidence in our models predictions. As shown with CH_2NH, the coupling between carbon and nitrogen chemistry combined with radicals produced by photolysis can have huge effects impacting the transmission spectra. This should be kept in mind when adding new elements like sulfur, as only adding a sub-mechanism neglects these coupling effects.

Key words. astrochemistry – planets and satellites: atmospheres – planets and satellites: composition – methods: numerical – methods: statistical

1. Introduction

Over recent decades, and still remaining relevant today, the characterization of the atmospheric composition of exoplanets has only been possible for massive hydrogen-dominated exoplanets close to their star. Because of the detection biases of the transit method and its technical difficulty for exoplanets with a shallow transit depth, the range of masses and semi-major axis that can be probed by spectrometric means remains blind to colder, Earth-like exoplanets. The proximity of these observable exoplanets to their star results in highly irradiated atmospheres (Linsky et al. 2013), which implies both a high temperature profile that activates endothermic reactions and an intense UV flux that photodissociates the majority of species in the upper atmosphere, resulting in the creation of a high quantity of radicals (Heays et al. 2017). This proximity also causes huge tidal forces that probably results in these exoplanets to be tidally-locked, which further intensifies the horizontal and vertical temperature gradients in the atmosphere, causing intense advection and strong steady winds (Menou 2022; Charnay et al. 2015). We also know that this advection coupled to photolysis in the upper atmosphere should maintain the chemical species abundance profiles in a steady-state out of equilibrium (Moses et al. 2011; Roudier et al. 2021; Stevenson et al. 2010). To take into account the dynamical timescale, it is therefore necessary to accurately describe both the atmospheric advection and the chemical kinetics of the reactions taking place in the atmosphere (Drummond et al. 2020; Zamyatina et al. 2023). Accurately reproducing the chemistry in these conditions requires a detailed kinetic network, which describes chemistry in sets of elementary reversible reactions that form, consume, and propagate radicals. These reactions then form a parameterized chemical network that can be used to model the chemical kinetics in exoplanet atmospheres. However, the parameters that characterize the kinetic properties of each reaction can be difficult to estimate and their determination is subject to an entire field of research in combustion kinetics (Wang & Sheen 2015; Curran 2019). In the combustion domain, the detailed kinetic networks are validated against experimental data measured in 0D or 1D reactors close to ideal reactors and designed to characterize only the chemical kinetics. Such data can include the evolution of combustion products and intermediates as a function of time or temperature, auto-ignition delay times, or laminar flame studies (Battin-Leclerc et al. 2011).

For atmospheric studies of exoplanets, various detailed kinetic networks have already been developed (Moses et al. 2011; Tsai et al. 2017, 2021; Venot et al. 2012, 2015, 2020; Rimmer & Helling 2016). Most of these chemical networks were built by grouping reactions with available parameters from databases and/or computed with quantum mechanics calculations. Venot et al. (2012, 2015, 2020) networks are the only ones based on networks validated by experiments. Venot et al. (2012) was the first one to be developed, and was extended to species bearing up to six carbon atoms in Venot et al. (2015). Additional corrections to the methanol chemistry were later introduced (Venot et al. 2020; hereafter Venot 2020). These networks usually describe only the kinetics of carbon-, hydrogen-, oxygen-, and nitrogen-bearing species, and are such labeled C/H/O/N chemical networks. In this present work, we aim to develop a new C/H/O/N network for exoplanet atmospheric chemistry based on extensive validations against experimental data, totally revisiting the C/H/O/N chemistry and basing it on two new state-of-the-art combustion networks for C/H/O and N chemistry, respectively, from Burke et al. (2016) and Glarborg et al. (2018).

To accurately reproduce very different conditions from warm sub-Neptunes to very hot Jupiters, with potential applications to warm super-Earths, the new chemical network is a detailed network suitable for a wide range of pressures and temperatures. The validity domain of the network must therefore be, in principle, from 500 to 2500 K and from 100 to 10^{-6} bar. The network is also required to accurately describe the kinetics of all C/H/O/N species with fewer than two atoms of carbon in order to correctly model the overall chemistry of every major species observed and potentially visible in exoplanet spectra (H_2O, CH_4, NH_3, CO, CO_2, HCN, C_2H_2, C_2H_4, C_2H_6 ...). Although the chemical network is aimed at studying hydrogen dominated atmospheres, it should remain valid at even very high metallicity and for every possible C/H/O/N atomic abundance. This implies that it should accurately describe all the reaction kinetics ranging from oxygen-poor, carbon-, and hydrogen-dominated atmospheres for pyrolysis, up to oxygen-rich environments, more favorable to oxidation reactions. Due to limitations in the available computational resources, it is mainly intended for 1D simulations.

Section 2, discusses how we selected the combustion networks with which we developed our new chemical network, the extensive validation that came along with it and the additions and modifications made to the original networks. Then, in Sect. 3, we apply this network to the study of exoplanet atmospheres. We studied four planets: GJ 436 b, GJ 1214 b, HD 189733 b, and HD 209458 b, and we compared our results with those obtained with the chemical network Venot 2020. We also investigated the differences between the two networks to highlight new chemical pathways, in addition to discussing potential repercussions on the transmission spectrum and their implications on the observability and reliability of current models to interpret JWST observations. Finally, we conclude in Sect. 4 and discuss potential future improvements on this work.

2. Detailed combustion network selection

2.1. Considered combustion networks

Seven networks validated on combustion experiments have been compared: NUIGMech1.1, AramcoMech3.0, Burke 2016, Exgas 2014, Konnov 2005, Glarbor 2008, and Venot 2020. The first three networks, NUIGMech1.1, AramcoMech3.0, and Burke 2016, have been developed by Curran et al. at the National

University of Ireland in Galway, which led the improvements of combustion kinetics in the last years.

NUIGMech1.1. Currently, NUIGMech1.1 (Wu et al. 2021) is the state-of-the-art kinetic network for C/H/O combustion. This network, that has been extensively validated against experimental data, describes the combustion kinetics of species up to molecules containing seven carbon atoms (C_7). It also contains nitrogen reactions for the chemistry of NO_x, which are regulated pollutants in combustion processes. This level of details to capture the chemistry of C_0-C_7 species is achieved at the cost of a very large network size (2746 species and 11 279 reactions).

Because of the large size of NUIGMech1.1, which makes it impractical for 1D calculations, two smaller C/H/O networks from the same team were also considered: AramcoMech3.0 and Burke 2016.

AramcoMech3.0. AramcoMech3.0 (Zhou et al. 2018) is a C/H/O C_4 network of 581 species and 3037 reactions that focuses on improving the simulations of Polycyclic Aromatic Hydrocarbon formation.

Burke 2016: Burke 2016 is a C/H/O C_3 network of 173 species and 1011 reactions (Burke et al. 2016), which aimed to better reproduce the combustion of methanol, involved in the combustion of biofuels.

To verify the performances of these networks, we included another network of the literature for C/H/O chemistry in our comparisons: Exgas 2014.

Exgas 2014. Exgas 2014 (Bounaceur et al. 2015) is a C/H/O C_3 network of 209 species and 1472 reactions generated with Exgas (Warth et al. 2000), a software that automatically generates combustion detailed kinetic networks. It was used to predict auto-ignition temperatures and delays for gas turbine applications.

Because all these networks besides NUIGMech1.1 lacked nitrogen chemistry, we included three other networks of the literature on C/H/O/N chemistry: Konnov 2005, Venot 2020, and Glarborg 2018.

Konnov 2005: Konnov 2005 is a C/H/O/N C_2 network of 127 species and 1213 reactions (Konnov et al. 2005) designed to study the oxidation of NO into NO_2 in a medium containing ethane and was part of the research effort to reduce NO_x emissions from car engines due to toxicity and pollution concerns.

Venot 2020: Venot 2020 is the Venot et al. (2020) chemical network, which is an updated version of the Venot et al. (2012) network from which the methanol chemistry was reevaluated. It was especially designed for the study of exoplanet disequilibrium chemistry. It is a C/H/O/N C_2 network of 112 species and 944 reactions, also derived from four experimentally validated combustion networks (Bounaceur et al. 2010; Konnov 2009; Dagaut et al. 2008a; Burke et al. 2016).

Glarborg 2018: Glarborg 2018 is a C/H/O/N C_3 network (Glarborg et al. 2018) that aimed at improving the precision of nitrogen chemistry, especially NO_x formation. It is a very comprehensive and widely used network for the modelling of nitrogen chemistry in combustion.

For clarity, all the networks used for comparison are listed in Table 1.

2.2. Experimental data

In order to select the best chemical network for our requirements, we gathered 1618 combustion experimental data points, tested

Table 1. Characteristics of the chemical networks considered and compared in this study.

Name	Species	Reactions	Size	Atoms
NUIGMech1.1	2746	11 279	C_7	C/H/O/N
AramcoMech3.0	581	3037	C_4	C/H/O
Exgas 2014	209	1472	C_3	C/H/O
Burke 2016	173	1011	C_3	C/H/O
Glarborg 2018	151	1397	C_3	C/H/O/N
Konnov 2005	127	1213	C_2	C/H/O/N
Venot 2020	112	944	C_2	C/H/O/N

Notes. Size corresponds to the heavier reactant included in the network.

the seven different networks over conditions detailed in Table A.1 using the Ansys software Chemkin-Pro (Kee et al. 2006), and, finally, we compared them to the experimental data. For a large majority, these data consisted in molar fraction measurements of different species (reactants and products, 1558 measurements out of 1618), but also in the measurement of auto ignition delay times (IDT, 60 measurements out of 1618). This delay corresponds to the time it takes for a fuel mixture to spontaneously ignite at a given temperature and pressure. In experiments, it is measured as the time between the moment when the gas is brought to temperature and pressure conditions and the moment when the ignition is detected. It is most often detected by a pressure or concentration peak of excited OH or CH radicals. In our simulations, the ignition delay time is chosen to be the time at the maximum concentration of the OH radical. These experimental data were collected over 21 different publications in total, from a wide range of conditions fully described in the appendix. The first eight experimental conditions considered were taken from those used in Venot et al. (2020), to determine how the other chemical networks compare to it on the original data used for its validation. The data collected for the first six experimental conditions consisted in the temporal evolution of the abundances of major species at play at the start and end of reaction (CH_3OH, O_2, CO, CO_2, H_2O, HCHO, H_2 ...) in three different reactor types (closed reactor, plug flow reactor, shock tube). The seventh consisted in the auto-ignition delay time measurement in a shock tube at an initial pressure of 10 and 50 bar, at 10 and 5 different initial temperatures, respectively, over a range of 1000 to 1300 K. For the eighth, it consisted in the evolution with temperature of abundances of major species at the exit of a perfectly-stirred reactor. The rest of the experimental conditions (9–21 in Table A.1) were focused on exploring a wider range of initial species and conditions by varying equivalence ratios, from very oxygen-rich combustion to pyrolysis, in addition to varying the fuel type, which consisted in combustion of H_2, of HCN, pyrolysis of CH_4, of C_2H_5OH, as well as reactions of nitrogen species like N_2O, NO, or NH_3. Like the eight first ones, these data consisted in auto-ignition delay times, abundances over time or abundances at steady state over temperature, and sometimes with a parameter study on equivalence ratio, pressure, or different initial species. The species concerned by these abundance data can be reactants (H_2, CH_4, HCN, C_2H_5OH, O_2 ...), products (H_2O, CO_2, CO, C_2H_2, C_2H_4, C_2H_6, CH_3CHO, HCHO ...) or appear as both in the data set depending on the conditions (CH_4, H_2).

In combustion conditions, the parameter describing the abundance of fuel to oxidizer is the equivalence ratio:

$$\phi = \frac{n_{\text{fuel}}/n_{\text{ox}}}{[n_{\text{fuel}}/n_{\text{ox}}]_{\text{sto}}},$$

with n_{fuel} as the fuel quantity, n_{ox} as the oxidizer quantity, and $[n_{\text{fuel}}/n_{\text{ox}}]_{\text{sto}}$ as the ratio of these values in a stoichiometric mixture. As the equivalence ratio grows larger, the fuel proportion gets higher and the combustion conditions get closer to pyrolysis conditions. Pyrolysis corresponds to high temperature conditions in a reducing medium with no oxygen, while combustion refers to high temperature conditions in an oxidizing medium, usually oxygen. Covering a wide range of equivalence ratios in our dataset allows us to test the kinetic networks on different compositions to ensure their ability to accurately model the chemistry occurring on exoplanets with very different elemental abundances. Pyrolysis and a high equivalence ratio combustion corresponds to low metallicities with high C/O, N/O, and H/O ratios, while a low equivalence ratio combustion corresponds to high metallicities with low C/O, N/O, and H/O ratios. In total, the full experimental data set spanned equivalence ratios from 0.05 to 5 and pyrolysis conditions, pressures from 0.2 to 50 bar and temperatures from 800 to 2400 K.

2.3. Error calculations

To test the agreement of the different chemical networks with the experimental data, network predictions were plotted against experimental points and compared. This resulted in over 500 plots, which is too much to be shown here. Therefore, we will focus on the distribution of errors for each chemical network, compiled in histograms of Fig. 1, and discuss the main tendencies visible in the overall dataset.

To sum up these numerous plots into a statistical distribution of errors shown in Fig. 1, we chose to compute these errors using the following formula:

$$y_{\text{error}} = \frac{y_{\text{mod}} - y_{\text{exp}}}{y_{\text{max}}},$$

with y_{exp} being the values of each experimental point in our dataset, y_{mod} being the network prediction at that point and y_{max} being the value of the highest experimental point over the experimental range. Each experimental point corresponds to a measurement of the molar fraction of a species (either product or reactant, for 1558 measurements out of 1618), but also of the IDT of a mixture (60 measurements out of 1618). Depending on the reactor type, for a given experimental range of measurements, pressure, temperature, or reaction time can change. This range depends on the type of data, and corresponds to the temperature range of the original measurements for temperature studies, and to the time range of the original measurements for mole fraction over time studies. This choice is done to give a relative error that can be compared between different experiments, while avoiding non-representative errors due to data points close to zero and experimental and pointing noise causing diverging relative errors. The assumed network prediction corresponds to the linear interpolation between the two closest computed points. For temperature studies, the computed points were evenly distributed over the experimental range, compromising between the density of the distribution and the computational time. For time studies, the computed points were determined by the software used for the calculations.

In these histograms, NUIGMech1.1, Burke 2016, and Glarborg 2018, display the models with the best prediction accuracy over the dataset. In the following, the focus is more on in-depth descriptions of the causes underlying these results. In total, over the 1618 experimental points, about 50 were beyond 100% calculated error for all models, with maximum values
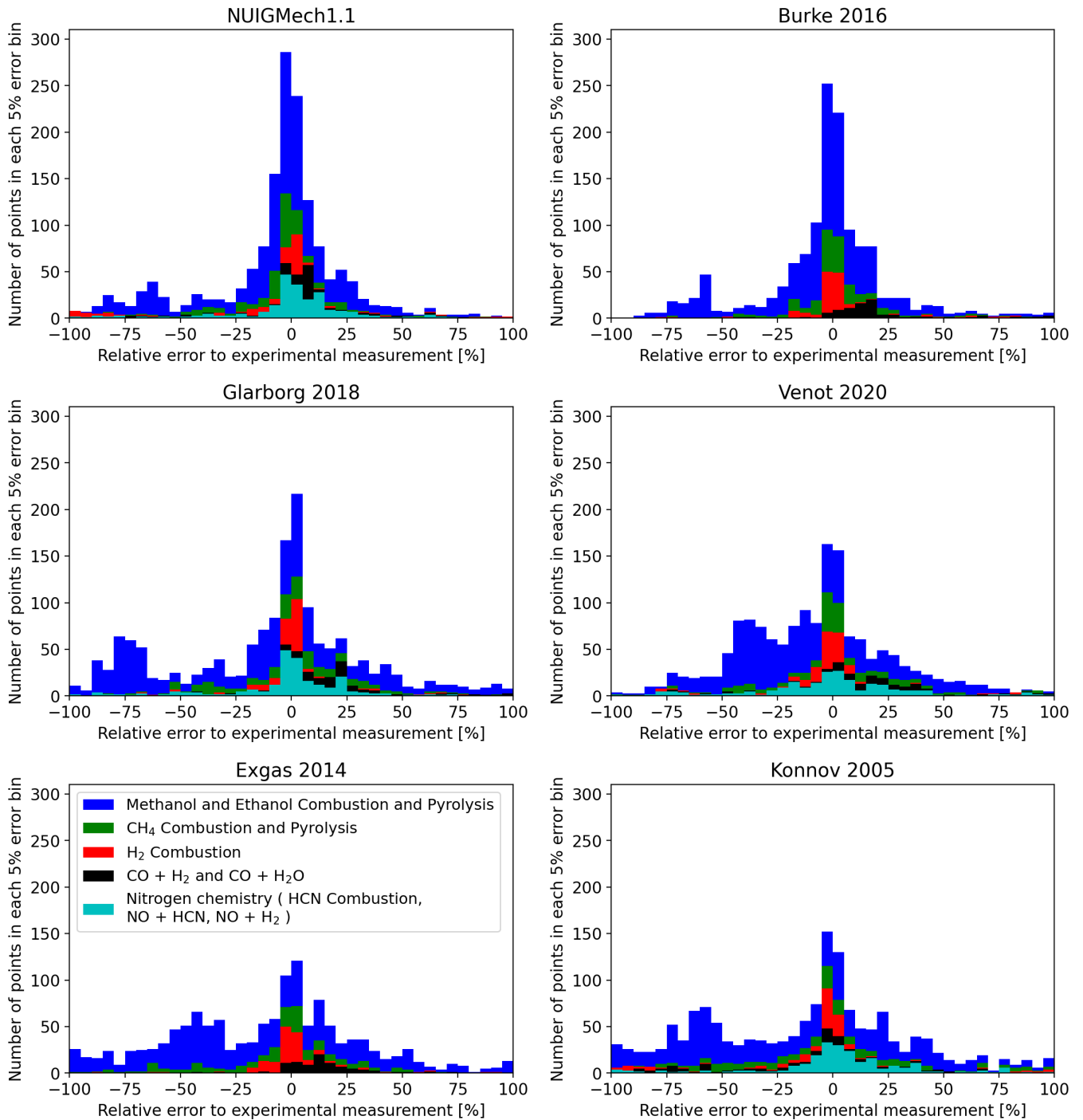
Fig. 1. Statistical distribution of the relative error over every experimental point in the 1618 points data set for each studied chemical network. Points are grouped in colors corresponding to a different type of initial conditions. AramcoMech3.0 is not shown here as it is almost identical to Burke 2016.

reaching around 2500%. These high deviations are found with all the chemical networks and were not plotted in error distributions. They mainly come from conditions 16, 17, and 18 in Table A.1 for ethanol and methane pyrolysis, the important discrepancies observed between experiments and simulations appearing for plug flow experiments. For these specific experiments, important shifts in time (or temperature) are observed which dramatically affect the y_{error} calculated. There is also an abnormal distribution of errors around −70% seen in Fig. 1 for all models, mainly coming from conditions 19 of Table A.1 and concerning C_2H_4 and H_2O. These errors could be due to issues in the experimental

points, for example, due to ethanol reacting before entering the reactor.

2.4. Auto ignition delay time

When first comparing the different plots for each network on methanol combustion (conditions 1–9 in Table A.1), the first thing that stood out was that the chemical networks based on the work of Curran and co-authors (AramcoMech3.0, NUIGMech1.1, and Burke 2016), were all way better at describing auto ignition delay times. They agree with the auto ignition
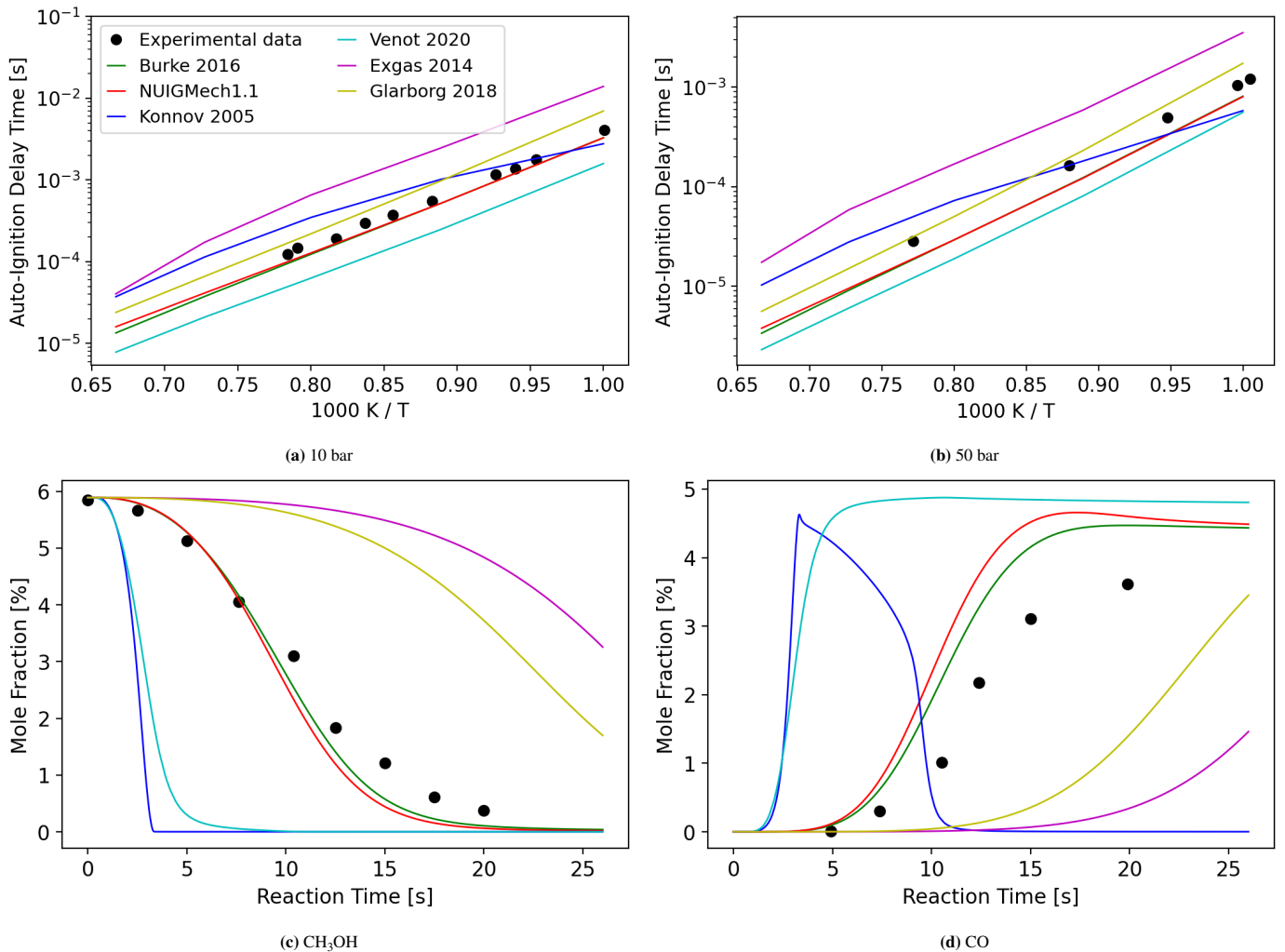
(a) 10 bar

(b) 50 bar

(c) CH$_3$OH

(d) CO

Fig. 2. Ignition delay time of methanol at 10 bar (a) and 50 bar (b) in condition 1 and mole fraction of CH$_3$OH (c) and CO (d) over time in condition 2 of Table A.1 for all tested chemical networks. AramcoMech3.0 is not shown here as it is almost identical to Burke 2016.

data of methanol shown in Figs. 2a and 2b with a mean error of 5% at 10 bar and within 10% at 50 bar, with almost no visible difference between them. On the contrary, the Exgas network severely overestimates this delay, with almost an order of magnitude difference. The Konnov network does not reproduce the temperature dependence: delays are underestimated at low temperatures (under 1050 K) and overestimated at high temperatures (over 1050 K) by around 150%. For the Glarborg network, the delay is overestimated at both pressures by around 30%, and for the Venot 2020, this delay is too short by around –40%. The ability of each network to accurately describe the auto ignition delay time in given initial conditions has major consequences on kinetic simulations of mole fraction over time. When a network underestimates the IDT, fuel consumption will tend to be overestimated. This correlation is clearly visible in our dataset. Figure 2a and 2b shows that Venot 2020 underestimates the IDT while Glarborg 2018 overestimates it. This is related to Fig. 2c, where CH$_3$OH consumption is overestimated for Venot 2020 and underestimated for Glarborg 2018. This impact is clearly seen in combustion conditions, as shown in Fig. C.1, leading to CH$_3$OH error distribution of Venot 2020 to be mostly between –100% and 0% error, and between 0 and 100% error for Glarborg 2018. Figure 2d shows that in consequence, products like CO tend to be overestimated around

ignition time for networks with underestimated IDT, as in Venot 2020, and, conversely, for networks with overestimated IDT like Glarbor 2018. As the oxidation of intermediate species like CO is not directly linked to IDT, other parameters may control CO consumption, as visible with Konnov 2005.

2.5. Combustion and pyrolysis of methanol, ethanol, formaldehyde, and acetaldehyde

Focusing on data related to methanol thermal decomposition, we can see in Fig. 3 that Exgas, Glarborg, and Konnov networks overestimate CH$_3$OH abundances profiles, while Venot 2020 tends to underestimate methanol abundances. Eventually, for these networks, their best performances on methanol points are for data in perfectly stirred reactors or plug flow reactors.

In addition, ethanol results are also displayed in Fig. 3. The experimental conditions concerning this species include only ethanol pyrolysis, with temperature- and pressure-dependent species profiles. CH$_3$CHO data come exclusively from these conditions (18 and 19 of Table A.1), whereas CH$_2$O errors also include methanol combustion experiments (2, 6, 7, and 8 of Table A.1). The Curran-based networks give quite similar results for these species, except for NUIGMech1.1 that is significantly better on methanol. This is probably due to a better
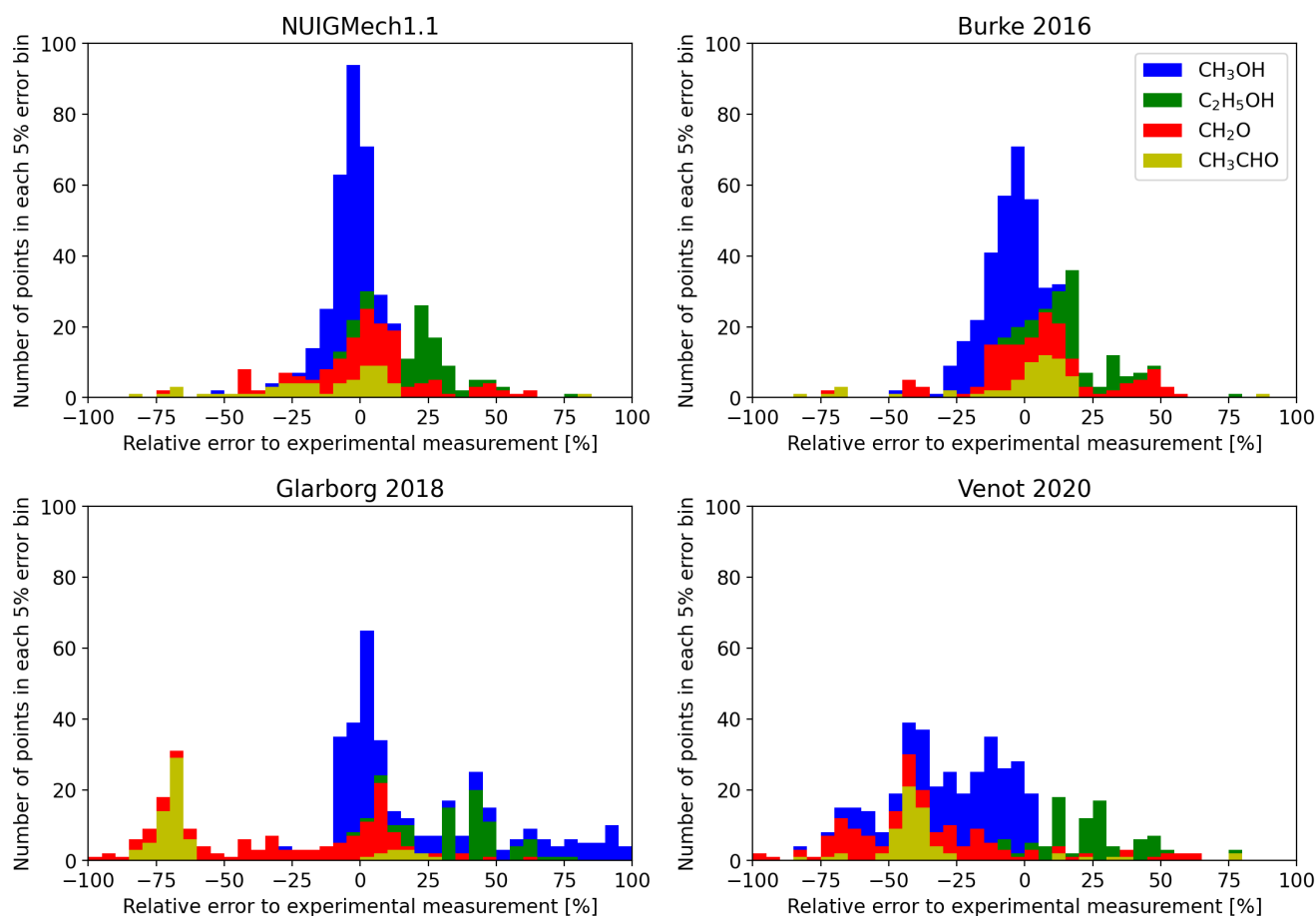
Fig. 3. Statistical distribution of the relative error over the 449 experimental data points for intermediate products (CH_3CHO, CH_2O) in combustion and pyrolysis of C_2H_5OH and CH_3OH. Each color gathers all molar fraction measurements of the corresponding species. Contribution from combustion and pyrolysis data are shown separately in Figs. C.1 and C.2.

representation of the growth mechanism towards heavier molecules occurring under pyrolysis conditions. Overall, these networks are similar over these species. The Glarborg network is accurate for methanol pyrolysis, but is less effective for methanol combustion. For C_2H_5OH, its performances are less accurate than the previous networks, and for CH_3CHO, experimental abundance is underestimated by about −75%. Venot 2020 also reproduce these experimental points quite badly, especially on CH_2O and CH_3CHO.

2.6. Main products and reactants in combustion and pyrolysis

Main species are shown in Fig. 4. This histogram gathers all computed errors of model predictions on experimental measurements (mole fraction and IDT) of H_2, CH_4, H_2O, O_2, CO, and CO_2 regardless of their role in the experiment (either product or reactant). In condition of combustion of H_2, all the networks were within 5% or 10% error. For H_2 mole fraction measurements coming from methane pyrolysis experiments however, almost every network underestimated its production compared to the experimental points, although the Curran-based networks were the closest to experiments. In ethanol pyrolysis, on the contrary, the H_2 production was severely overestimated by all the networks, especially at high temperatures, with errors up to 200% at 1300 K with usually reliable networks like NUIGMech1.1.

For methane pyrolysis, the Curran-based networks were under 5% error, while other networks like Exgas or Venot 2020 overestimated CH_4 abundances by around 20%. For methane combustion, almost all networks were under the 5% error range except for the Konnov network whose temperature dependence was totally off. On ethanol pyrolysis conditions, methane production were underestimated by all networks.

For water, results were good for all the networks, except in the ethanol pyrolysis conditions, where H_2O production was severely underestimated by all the networks by around 75%, which is shown as red bars in Fig. C.2.

For O_2 consumption in methanol or hydrogen burning conditions, the best networks were the Curran-based networks, with the same problems as noted previously for others, which were due to bad methanol ignition delay time predictions.

One species that displayed significant gains in accuracy with the Curran-based networks is CO, which has a wide range of errors with such networks as Exgas 2014, Glarborg 2018, Konnov 2015, and Venot 2020. However, for CO_2, we do not see a significant improvement over our dataset in relation to these experimental data.

2.7. Network base choice and C₂ reduction

To derive our C/H/O/N chemical network from these combustion networks, multiple options were considered. The first one was to simply take the Glarborg 2018 network, as it is already
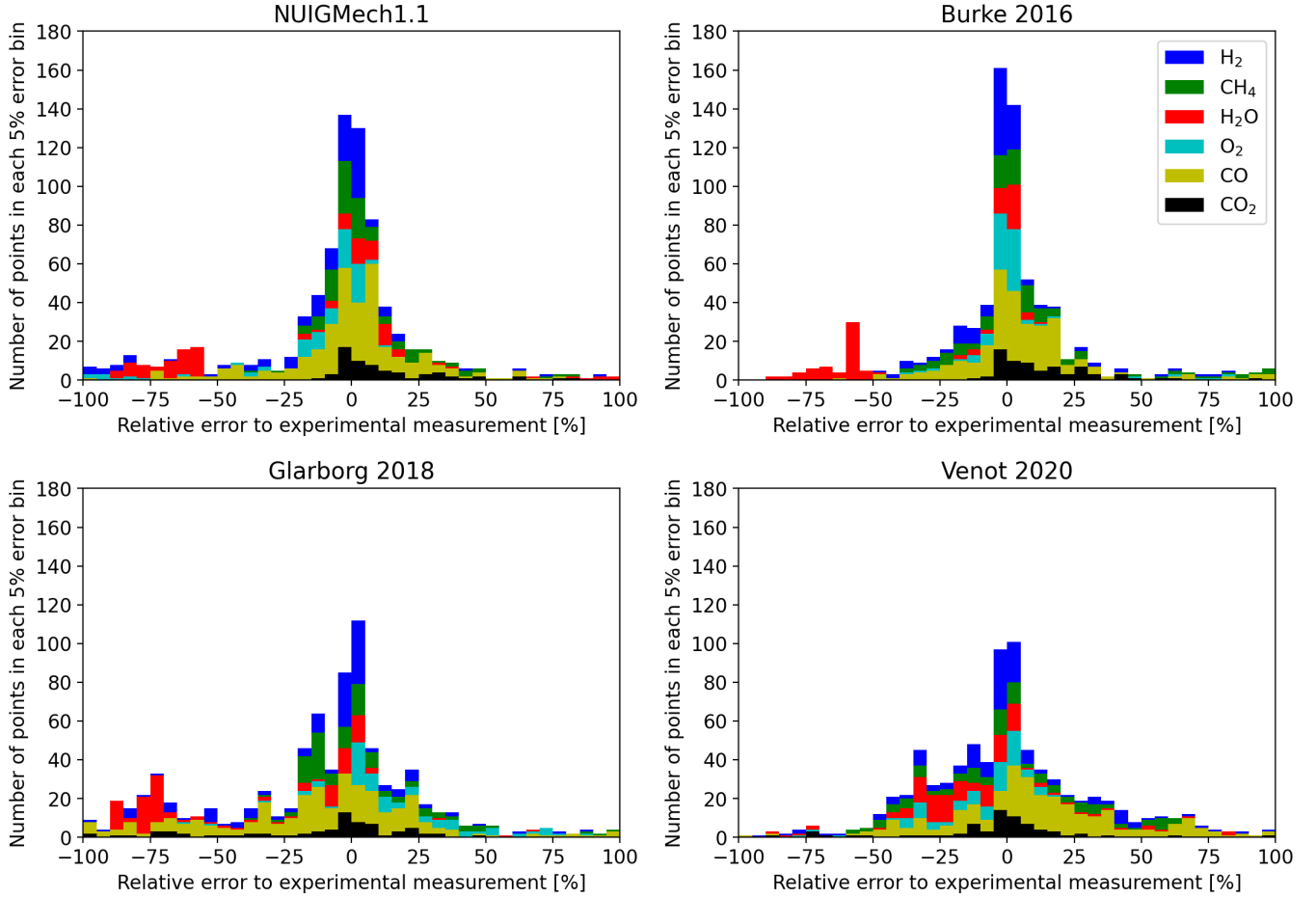
Fig. 4. Statistical distribution of the relative error over the 823 experimental data points for the main pyrolysis products (H_2, CH_4), combustion products (H_2O, CO, CO_2), and reactants (O_2) in combustion and pyrolysis of CH_3OH, CH_4, H_2, HCN, and C_2H_5OH. For some points, CO and H_2O are reactants (condition 13 of Table A.1). Each color gathers all molar fraction measurements of the corresponding species. Contribution from combustion and pyrolysis data are shown separately in Figs. C.3 and C.4.

a C/H/O/N network. However, as seen in the corresponding error distributions in Figs. 1 and 3, this network performance, although better than older networks like Venot 2020 or Konnov 2005, is surpassed by the oxygenated species and alcohol combustion conditions of recent methanol-focused networks, such as Burke 2016, or the generic state-of-the-art network NUIG-Mech1.1. However, with respect to the nitrogen chemistry, it is the most state-of-the-art network, although the difference with NUIGMech1.1 and Konnov 2005 was not shown very clearly in our dataset. In the end, as both nitrogen and C/H/O chemistry are equally important for exoplanets, we decided to fuse the Glarborg 2018 network with the Burke 2016 network, keeping both the most state-of-the-art chemistry network with the best performing reasonable sized network on our data, while making sure that the methanol chemistry is accurate. To further reduce our network size, we first removed 81 out of 91 species from the C_3 sub-mechanism of Burke 2016 and their reactions, but kept the last 10 that were necessary to preserve the accuracy on some C_2 species. This reduction was made because for exoplanets, C_3 species abundances are usually low and their interest is limited in comparison to the increase in computation time they require due to the higher number of possible isomers. In addition, limiting calculation times allows for future additions of other species such as sulfur and its use in retrievals using TauREx with the FRECKLL plugin.

2.8. Additional modifications to the network

While applying our chemical network to exoplanet studies, we noted that NH_3 formation at high altitudes was primarily driven by a reversed globalized reaction: $CH + NH_3 \longrightarrow H_2CN + H + H$. This reaction was assumed to be the combination of two reactions: $CH + NH_3 \longrightarrow CH_2NH + H$ and $CH_2NH \longrightarrow H_2CN + H$, but was written in this compact form in the original network of Glarborg 2018, implicitly assuming that the latter reaction would always happen only after the former. This simplification (while certainly reasonable in nitrogen combustion chemistry) is not suited to exoplanetary conditions, especially in the upper atmosphere, where photolysis combined with low density conditions maintains a really high concentration of hydrogen radicals that heavily favors the reverse reaction, resulting in an unphysical NH_3 production pathway. Hence, we decided to rewrite the reversible reaction $CH + NH_3 \rightleftharpoons H_2CN + H + H$ into two others: $CH + NH_3 \rightleftharpoons CH_2NH + H$, for which we kept the parameters of the $CH + NH_3 \rightleftharpoons H_2CN + H + H$ reaction, and $H_2CN + H \rightleftharpoons CH_2NH$. For this second reaction, the choice of parameters was based on the reaction $NH_2 + H \rightleftharpoons NH_3$ by analogy. Both reactions are indeed the recombination of a nitrogen radical with a hydrogen atom, and therefore occur with no activation energy. They also should share a similar pre-exponential factor, with no temperature dependence. This

Table 2. Different added reactions to the network and their parameters.

Reaction	A	n	E	Analogy for A and n	Source for E
$NH_2 \xrightarrow{+M} NH + H$	5.6×10^{15}	0	96 600	$CH_2 \xrightarrow{+M} CH + H$ (Bauerle et al. 1995)	$\Delta_r H$
$C + NH \rightleftharpoons CN + H$	5.0×10^{13}	0	0	$C + OH \rightleftharpoons CO + H$ (Glarborg et al. 1986)	N/A
$N + H \xrightarrow{+M} NH$	4.7×10^{18}	−1	0	$O + H \xrightarrow{+M} OH$ (Tsang & Hampson 1986)	N/A
$CN \xrightarrow{+M} C + N$	1.5×10^{16}	0	180260	$C_2 \xrightarrow{+M} C + C$ (Kruse & Roth 1997)	$\Delta_r H$
$NO \xrightarrow{+M} N + O$	1.5×10^{16}	0	150920	$C_2 \xrightarrow{+M} C + C$ (Kruse & Roth 1997)	$\Delta_r H$
$N_2 \xrightarrow{+M} N + N$	1.5×10^{16}	0	225940	$C_2 \xrightarrow{+M} C + C$ (Kruse & Roth 1997)	$\Delta_r H$

Notes. Values are in mol, cm^3, cal, s. Also, A, n, and E are the parameters of the modified Arrhenius equation, while $\Delta_r H$ is the enthalpy of formation of the reaction, whose values are taken from NIST. As C + NH and N + H are radical–radical combinations, they are barrierless reactions ($E = 0$). +M indicates low pressure limit reactions.

factor was hence estimated at 1.6×10^{14} cm^3 mol^{-1}s^{-1}. However, this value is only accurate in the high pressure limit because at low pressures, this reaction needs a third body to stabilize the product, causing a strong pressure dependence of the rate constant. Further work is needed to correctly take into account this pressure dependence, using advanced Variational Reaction Coordinate-VTST and Master Equation methods (Klippenstein 1992; Georgievskii & Klippenstein 2003a,b). We discuss the impact of this approximation in Sect. 3.2.2.

In addition, we disabled the reversibility of 24 other globalized reactions yielding three products, to prevent similar unexpected chemical pathways from occurring. However, we did not find any conditions resulting in the reverse direction of these reactions to be favored.

To further improve the reliability of the chemical network in the upper atmosphere, we searched for possibly missing radical reactions in the network that could significantly impact chemistry for these specific conditions. We listed all the major species and radicals typically encountered in exoplanets or produced by photolysis and checked for their reactions with N and NH radicals. Many reactions of N and NH are negligible in usual combustion conditions; hence, the coupling between all radicals is not systematic, especially with radical compounds such as NH. In exoplanets, the photochemistry of NH_3 produces a lot of N and NH radicals, in a medium where radicals are especially abundant, which causes them to mainly react between each other through pathways that may be usually neglected. While searching for these kinds of reactions, we identified six potentially missing reactions and determined their parameters by analogy with other reactions. These added reactions were also checked to ensure that they do not exceed the theoretical collision limit (see Table 2). We compared the chemical network results on our combustion data set before and after these modifications, confirming that it did not affect the network performances. This scheme can be downloaded from the KInetic Database for Astrochemistry (Wakelam et al. 2012)[1] and also from the ANR EXACT website[2].

3. Application to exoplanetary atmospheres

3.1. Models and data sources

Our prime motivation for this extensive work on combustion networks was to develop a very robust scheme for the study

of exoplanetary atmospheres. Thus, in this section, we now apply this new scheme to model the atmospheric chemical composition of various exoplanets. Our new C/H/O/N scheme was tested against multiple exoplanet cases and compared to the one published in Venot et al. (2020). In the following, we refer to the Venot 2020 chemical network as V20 and to our update as V23.

In order to span different type of hydrogen-dominated atmospheres, we chose to model GJ 436 b and GJ 1214 b (warm Neptunes) as well as HD 209458 b and HD 189733 b (hot Jupiters) using the same thermal profiles, initial conditions, and parameters given in Venot et al. (2020; Table 3). For each planet, we compared the abundances obtained with both V23 and V20. We calculated the chemical abundance profiles using FRECKLL (Al-Refaie et al. 2022b), which is the Python version of the code used in Venot et al. (2020). The results obtained with this code are identical, but the computational time has been greatly improved. The thermal profiles are discretized in a 130-layers grid, evenly distributed in pressure log space. We assumed a solar metallicity for HD 189733 b and HD 209458 b, a 100x solar metallicity for GJ 1214 b and both metallicities for GJ 436 b. Elemental abundances were based on Lodders (2010), with 20% less oxygen to account for sequestration in refractory elements.

We updated the photodissociation data (cross-sections and branching ratios, Table B.1), compared to that used in V20. To discriminate the changes due to this update and to chemistry, we first compared the abundance profiles of each exoplanet model for some of the major species (H_2, H_2O, CH_4, CO, N_2, NH_3, CO_2, HCN, and H) between the old photolysis and the new photolysis data for the V20 chemical network with FRECKLL. This update turned out to have little impact on photochemistry for most species on hot Jupiters (HD 189733 b and HD 209458 b) and for all species on warm Neptunes (GJ 436 b and GJ 1214 b). However, for HCN, the addition of two new photodissociation pathways of NH_3 into NH ($NH_3 \longrightarrow NH + H + H$ and $NH_3 \longrightarrow NH + H_2$) creates differences of up to one order of magnitude in the upper atmosphere of HD 189733 b and HD 209458 b between 10^{-6} and 10^{-7} bar. The consequences of this photolysis update are summarized in Fig. B.1.

In the following, we compare the chemical abundances obtained with V20 and V23 for each planet case, using only this most recent UV cross-section data and branching ratios. We also investigate on the reasons explaining the observed differences and identify the main chemical pathways at play in each network. To evaluate the impact on observables, we generated the transmission spectrum of every planet with TauREx 3.1

---

[1] https://kida.astrochem-tools.org/
[2] https://www.anr-exact.cnrs.fr/fr/chemical-schemes/

Table 3. Exoplanets simulated with V20 and V23 and input parameters used.

Planet name	Planet type	Star type	D (UA)	R (R_J)	T (K)	K_{zz} (cm^2 s^{-1})	M (solar)
GJ 436 b	Warm Neptune	M3V	0.029	0.38	1094	10^9	1
GJ 436 b	Warm Neptune	M3V	0.029	0.38	1094	10^9	100
GJ 1214 b	Warm Neptune	M4.5V	0.014	0.24	1054	$3 \times 10^7 \times P^{-0.4}$	100
HD 189733 b	Hot Jupiter	K2V	0.031	1.14	1470	profile	1
HD 209458 b	Hot Jupiter	F9V	0.047	1.38	1671	profile	1

Notes. Here, D is the distance to the host star, R the planet radius, T the temperature at 1 bar, K_{zz} the eddy diffusion coefficient, and M the metallicity relative to solar abundances.
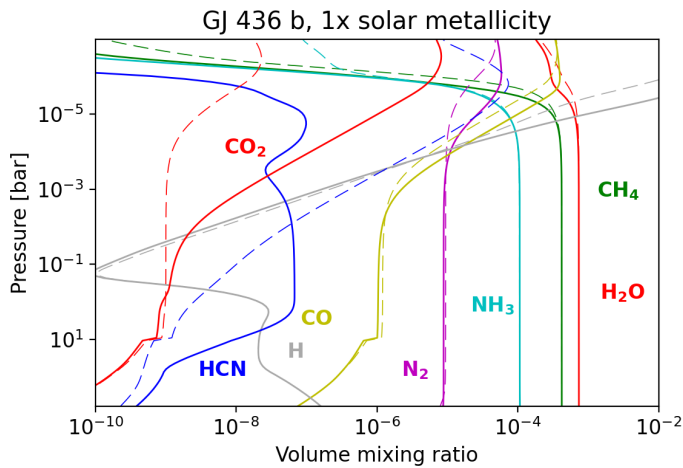
Fig. 5. Abundance profiles of GJ 436 b for solar metallicity and a constant eddy diffusion coefficient of 10^9 cm^2 s^{-1}. Dashed lines are for V20, while solid lines are for V23. H$_2$ is not shown to focus on other species, but its abundance profile in V23 is almost identical to V20.

Fig. 6. Total reaction rate profile for CO$_2$ in GJ 436 b with a solar metallicity with V20 (dashed lines) and V23 (solid lines).

(Al-Refaie et al. 2021), using a spectral resolution of 50 and opacities data from ExoMol (Tennyson & Yurchenko 2012) for HCN and from Al-Refaie et al. (2022a) for CH$_4$, CO, CO$_2$, H$_2$O, and NH$_3$. Rayleigh diffusion for CH$_4$, CO, CO$_2$, H$_2$, H$_2$O, He, N$_2$, and NH$_3$ as well as collision-induced absorption from HITRAN (Gordon et al. 2022) for H$_2$-H$_2$ and H$_2$-He were also included.

3.2. Results for GJ 436 b

For the warm Neptune GJ 436 b, we first simulated the 1D chemical abundance profiles assuming a solar metallicity and a constant eddy diffusion coefficient of 10^9 cm^2 s^{-1}. While some of the main species (H$_2$O, CH$_4$, NH$_3$, N$_2$, CO, and H) are found to have similar abundance profiles (Fig. 5) with both networks, we observe that two species differ by various orders of magnitude: CO$_2$ below 0.1 bar, and HCN on the whole pressure profile (100–10^{-7} bar). In the upper atmosphere, the molar fraction of CO$_2$ is higher with V23 than in V20, with a difference up to three orders of magnitude around 10^{-6} bar. For HCN, its molar fraction is lower in V23 than in V20 for pressures under 10^{-2} bar, with a difference of up to four orders of magnitude around 10^{-6} bar. For pressures higher than 10^{-2} bar, HCN molar fraction is higher in V23 than in V20, with a difference of up to two orders of magnitude around 10 bar. In the following, we discuss the origin of the differences for these two species.
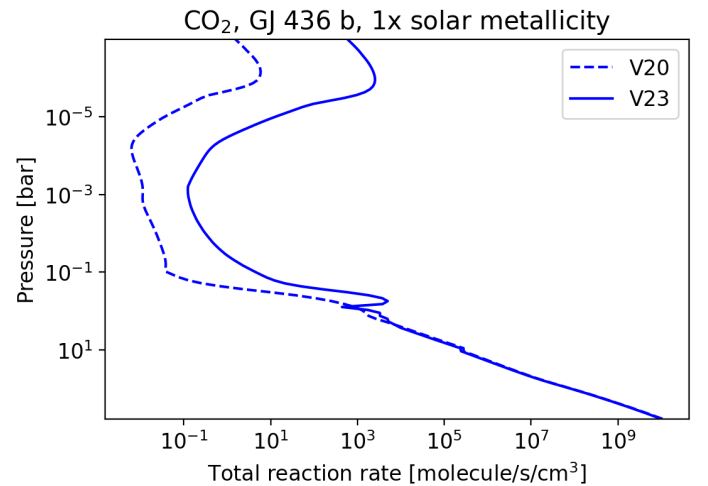
3.2.1. CO$_2$ differences

Upon investigating the reasons of this discrepancy, we found that between V23 and V20, the total CO$_2$ reactions rate profile was different. Figure 6 shows the total rate of CO$_2$ formation and destruction in each layer, which are equal when including vertical mixing because the profiles are at steady state. We see that these total reaction rates are larger below 1 bar with V23 than with V20.

Figure 7 presents the main contributions of each reaction to this total rate, the sum of positive contributions, and the sum of negative contribution both being equal to the total reactions rate when accounting for vertical mixing because of the steady state. For V23, Fig. 7 shows that the reaction CO + OH $\longrightarrow$ CO$_2$ + H is always the main CO$_2$ production reaction above 1 bar and the main CO$_2$ destruction reaction below 1 bar. Vertical mixing mainly transports the CO$_2$ produced in the middle atmosphere (1–10^{-3} bar) towards the lower atmosphere (below 1 bar), where it is destroyed into CO and OH through the CO$_2$ + H $\longrightarrow$ CO + OH reaction. For V20, this reaction is not the main destruction pathway of CO$_2$ in the lower atmosphere and needs the vertical mixing to compensate for the destruction of CO$_2$ through the N(^{4}S) + CO$_2$ $\longrightarrow$ NO + CO reaction, although it also remains the main CO$_2$ production reaction for pressures lower than 1 bar. At the peak of CO$_2$ abundance around 10^{-6} bar, the main production reaction is CO + OH $\longrightarrow$ CO$_2$ + H and the main loss mechanism is by photodissociation into CO through CO$_2$ $\longrightarrow$ CO + O(^{1}D), for both V20 and V23. Photodissociation rate being proportional to the CO$_2$ concentration,
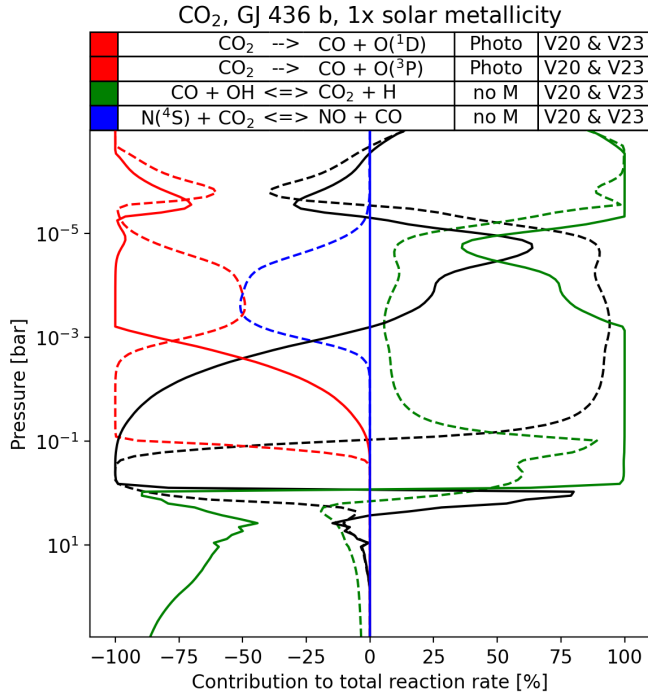
Fig. 7. Contribution profile of most major production and loss reactions for CO_2 in GJ 436 b. Positive values are production contributions and negative values are loss contributions. Black lines correspond to vertical mixing compensation, such as the sum in each layer is always zero due to steady state. Dashed lines are for V20, while solid lines are for V23. The contribution of photodissociation pathways to $O(^3P)$ and $O(^1D)$ are combined, $O(^3P)$ being favored above 10^{-5} bar and $O(^1D)$ being favored for lower pressures. The third column in the legend indicates the reaction type. "Photo" corresponds to photodissociations and "no M" corresponds to reactions without pressure dependence. The last column indicates which model includes this reaction.

its rate increase is directly linked to the higher CO_2 levels in V23. The UV cross-sections used in V23 and V20 being the same in these simulations, there is no difference in the main loss reaction parameters at this pressure between the two chemical networks, thus, this difference must come from the production reaction $CO + OH \longrightarrow CO_2 + H$. In V20, this production reaction is taken from Baulch et al. (1994) with the pre-exponential factor divided by 6, resulting in a production rate of around 5 molecule $cm^{-3} s^{-1}$ around 10^{-6} bar. In V23, these reaction parameters are taken from Joshi & Wang (2006), where it is treated as a sum of two modified Arrhenius equations, both having opposite temperature dependence. This results in a total production rate of around 2500 molecule $cm^{-3} s^{-1}$, which is three orders of magnitude greater than V20. This difference is directly observed in the rate constant of this reaction for the two networks and is fully attributable to the very different parameters used for modeling this reaction, as shown in Fig. 8. This difference has already been pointed out by Tsai et al. (2021) for temperatures in the 250–2000 K range (their Fig. 41). As for other combustion networks, such as Konnov 2005 or NUIGMech1.1, they are on a similar order of magnitude as V23 and also three orders of magnitude greater than V20, even using different sources for the reaction parameters. NUIGMech1.1 is particularly close to V23 for pressures around 100 bar and temperatures above 500 K, despite using data from Senosiain et al. (2005) and a single reaction with pressure dependent parameters. For temperatures below this value, some care should be taken as reaction rates differences between chemical networks raise above one order of
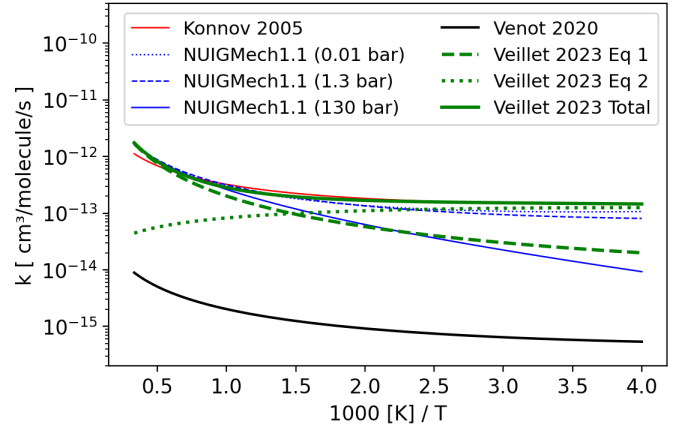
Fig. 8. Reaction rates of the reaction $CO + OH \longrightarrow CO_2 + H$ in V20 compared to V23, NUIGMech1.1, and Konnov 2005. In V23, this reaction rate is expressed as the sum of two modified Arrhenius equations (Eqs. (1) and (2)). In NUIGMech1.1, the rate constant is pressure-dependent.
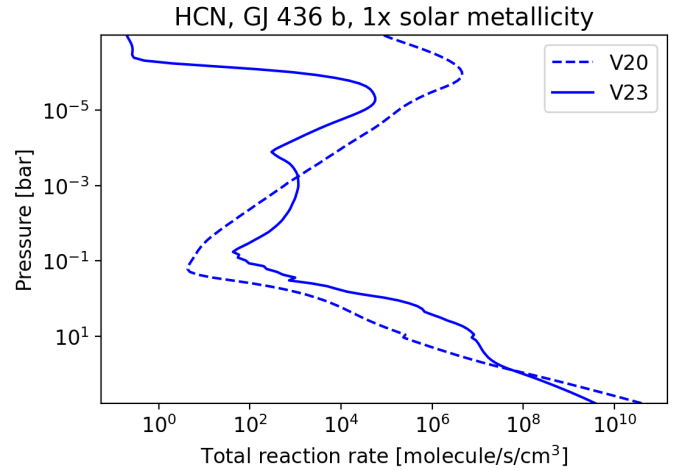

Fig. 9. Total reaction rate profile for HCN in GJ 436 b with a solar metallicity with V20 (dashed lines) and V23 (solid lines).

magnitude around 250 K, where the validity of these networks is no longer ensured.

3.2.2. HCN differences

We focus in this part in the differences observed between V23 and V20 for HCN. The total reaction rate profile for HCN production and consumption is shown in Fig. 9, and the respective contributions of major reactions are shown in Fig. 10. As expected, the HCN total reaction rate profile roughly matches the differences in HCN abundance, with the total reaction rate in V20 being up to six orders of magnitude higher than in V23 around 10^{-7} bar, and up to one order of magnitude lower between 100 and 10^{-3} bar. In both networks, the main production reaction between 10^{-2} and 10^{-6} bar is the reaction $HCN + H \rightleftharpoons H_2CN$. This reaction is implemented in V23 with a pressure dependent rate, with parameters interpolated in log space (PLOG) between 3 pressure values at 10, 1, and 0.1 bar. In V20, this reaction is described as two separate reactions: one for the high pressure limit, and one for the low pressure limit, requiring a third body. The parameters of the high pressure limit reaction are close to the values in the V23 PLOG reaction for 0.1 bar, and the low
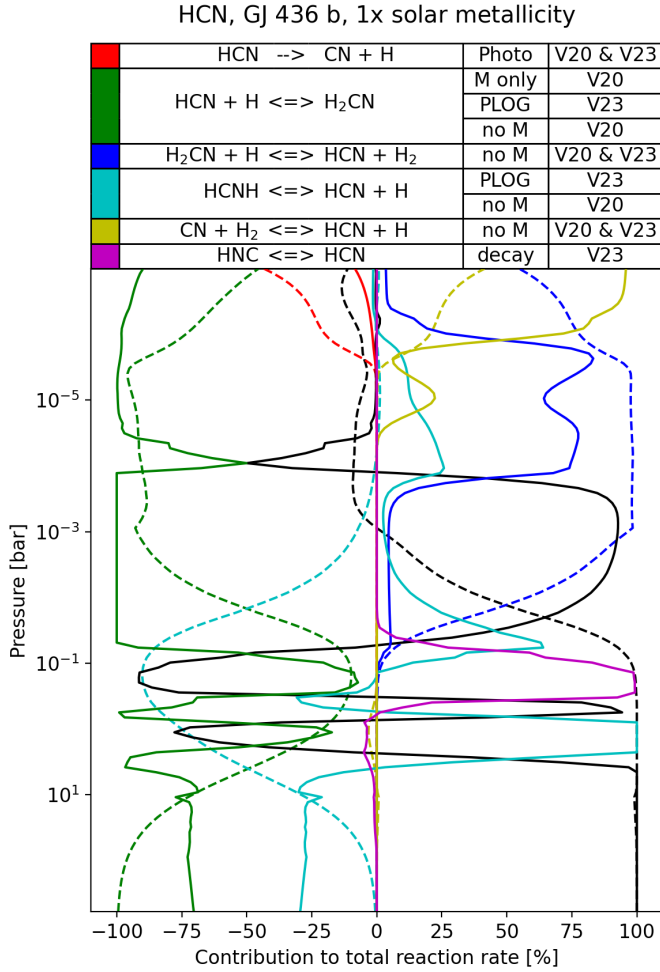
HCN, GJ 436 b, 1x solar metallicity

🟥	HCN --> CN + H	Photo	V20 & V23
🟩	HCN + H <=> H₂CN	M only	V20
		PLOG	V23
		no M	V20
🟦	H₂CN + H <=> HCN + H₂	no M	V20 & V23
🟦	HCNH <=> HCN + H	PLOG	V23
		no M	V20
🟨	CN + H₂ <=> HCN + H	no M	V20 & V23
🟪	HNC <=> HCN	decay	V23

Fig. 10. Contribution profile of most major production and loss reactions for HCN in GJ 436 b. Positive values are production contributions and negative values are loss contributions. Black lines correspond to vertical mixing compensation, such as the sum in each layer is always zero due to steady state. Dashed lines are for V20, while solid lines are for V23. The third column in the legend indicates the reaction type. "No M" corresponds to reactions without pressure dependence, "PLOG" to full pressure dependence and fall off description with PLOG formalism, "M only" to pressure dependence without fall off nor high pressure limit and "decay" to reversible, pressure dependent unimolecular reactions such as isomerization or electronic decay. The last column indicates which model includes this reaction.

pressure limit contribution decreases with altitude, becoming negligible for pressures below 0.1 bar. Therefore, these differences cannot explain those between the two HCN abundance profiles. It is also important to note that this description likely overestimates the HCN + H $\longrightarrow$ H₂CN reaction rate for pressures below 0.1 bar, for both networks. A PLOG implementation on the full pressure range (1000–10⁻⁸ bar) would be necessary to describe the full pressure dependence. In both networks, the main HCN production reaction is H₂CN + H $\longrightarrow$ HCN + H₂ between 0.1 and 10⁻⁶ bar. The parameters for this reaction are identical between the two networks, therefore it is not responsible for the differences between HCN abundance profiles. The other major contributing reaction, HCN + H $\longrightarrow$ HCNH is similar to the reaction HCN + H $\longrightarrow$ H₂CN, but results in the formation of HCNH, an isomer of H₂CN. V23 uses similar values to V20 for this reaction, although the pressure dependence

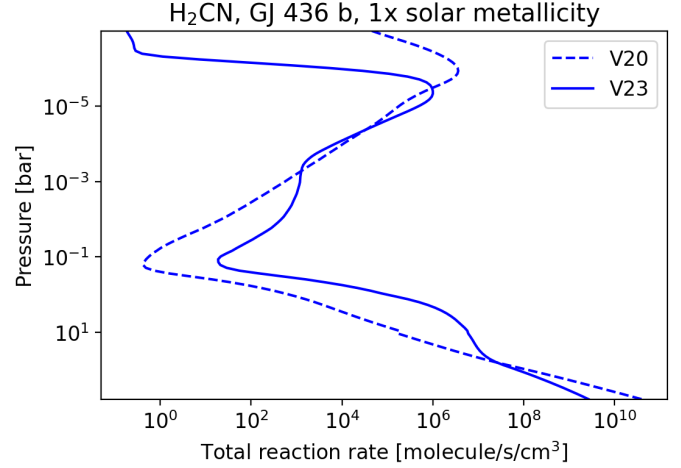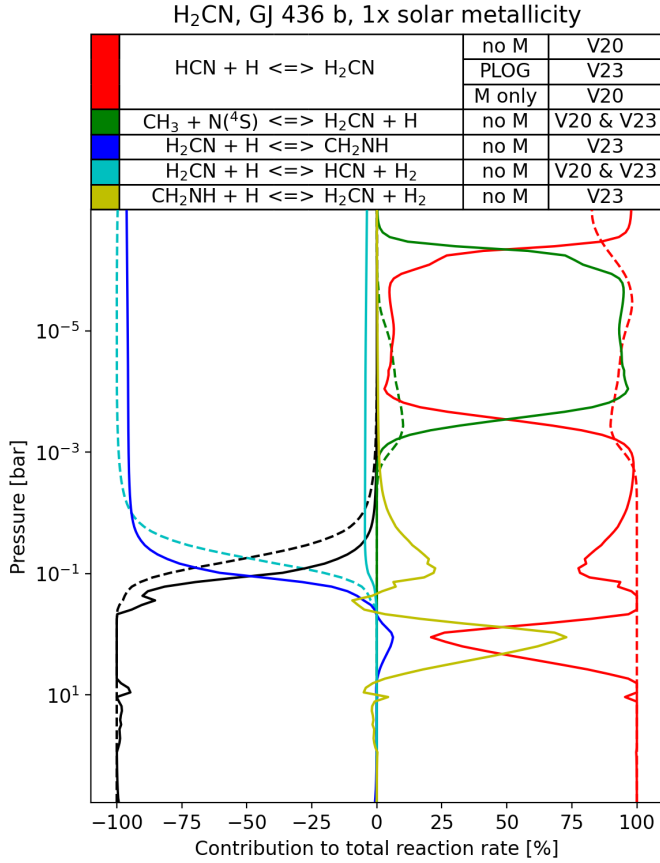## H₂CN, GJ 436 b, 1x solar metallicity

Fig. 11. Total reaction rate profiles for H₂CN in GJ 436 b with a solar metallicity with V20 (dashed lines) and V23 (solid lines).

is described between 0.1 and 10 bars with the PLOG formalism. Another difference between V20 and V23 is the inclusion of HNC in V23 and its isomerization reaction HNC $\rightleftharpoons$ HCN. However, this reaction does not impact HCN profiles, which we confirmed by running the simulation with V23 without this reaction. The combination of the reactions HCN + H $\longrightarrow$ H₂CN and H₂CN + H $\longrightarrow$ HCN + H₂ results in an equilibrium between the species HCN and its radical H₂CN. Hence, HCN differences between V23 and V20 are directly driven by production and consumption rate differences of H₂CN, which are shown in Fig. 11. As expected, we observe a similar reaction rate profile to HCN, with a total reaction rate up to six orders of magnitude above V20 for V23 at 10⁻⁷ bar, and up to two orders between 10 and 10⁻³ bar. This indicates that HCN abundance is mainly controlled by H₂CN abundance and its associated consumption and production reactions. Figure 12 shows a few differences on the major reactions of H₂CN. Firstly, in V20, the main consumption reaction on the whole pressure range is the reaction H₂CN + H $\longrightarrow$ HCN + H₂, previously mentioned as the main HCN production reaction in both networks that controls the HCN/H₂CN equilibrium. For pressures above 10⁻¹ bar, H₂CN consumption is not local anymore, and the vertical mixing advects H₂CN to be consumed in the upper layers by the reaction H₂CN + H $\longrightarrow$ HCN + H₂. Conversely, in V23, this reaction is negligible, and H₂CN consumption is entirely driven by the reaction H₂CN + H $\longrightarrow$ CH₂NH, discussed in Sect. 2.8. This difference is crucial, because the CH₂NH species and its linked reactions are absent from V20. Secondly, in V20, in the pressure range 10⁻⁴ to 10⁻⁶ bar, the main H₂CN production reaction is HCN + H $\longrightarrow$ H₂CN, which is the second mentioned reaction controlling the HCN/H₂CN equilibrium. In V23, the main reaction in this range is the reaction CH₃ + N(⁴S) $\longrightarrow$ H₂CN + H, that is included in both networks using the same parameters. Finally, in V23 at around 1 bar, the reaction CH₂NH + H $\longrightarrow$ H₂CN + H₂ becomes dominant for H₂CN production. This reaction opposes the H₂CN + H $\longrightarrow$ CH₂NH reaction, and reverts CH₂NH back to H₂CN. To better understand the role each of each reaction on the differences observed in the HCN abundance profile, we ran these simulations with modified versions of the V23 network presented in Fig. 13. This figure shows that disabling the reaction H₂CN + H $\longrightarrow$ CH₂NH results in a HCN profile almost identical to V20 (dashed and dash-dotted lines) for pressures lower than 10⁻¹. For pressures above this value however,

H$_2$CN, GJ 436 b, 1x solar metallicity

🟥	HCN + H <=> H$_2$CN	no M	V20
		PLOG	V23
		M only	V20
🟩	CH$_3$ + N(^{4}S) <=> H$_2$CN + H	no M	V20 & V23
🟦	H$_2$CN + H <=> CH$_2$NH	no M	V23
🟦	H$_2$CN + H <=> HCN + H$_2$	no M	V20 & V23
🟨	CH$_2$NH + H <=> H$_2$CN + H$_2$	no M	V23

Fig. 12. Contribution profile of most major production and loss reactions for H$_2$CN in GJ 436 b. Positive values are production contributions and negative values are loss contributions. Black lines correspond to vertical mixing compensation, such as the sum in each layer is always zero due to steady state. Dashed lines are for V20, while solid lines are for V23. The third column in the legend indicates the reaction type. "no M" corresponds to reactions without pressure dependence, "PLOG" to full pressure dependence and fall off description with PLOG formalism and "M only" to pressure dependence without fall off nor high pressure limit. The last column indicates which model includes this reaction.

GJ 436 b, 1x solar metallicity
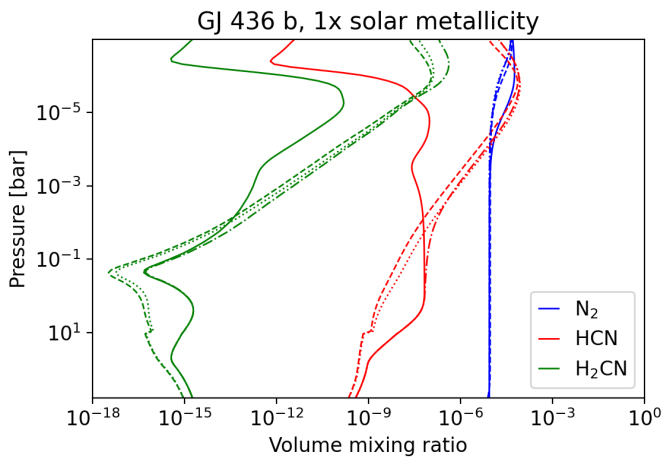
Fig. 13. Abundance profile of N$_2$, HCN and H$_2$CN with V23 (solid lines), V20 (dashed lines), V23 without the reaction H$_2$CN + H ⟶ CH$_2$NH (dashdot lines) and V23 without H$_2$CN + H ⟶ CH$_2$NH, CH$_2$NH + H ⟶ H$_2$CN + H, CH$_2$NH + CH$_3$ ⟶ H$_2$CN + CH$_4$, CH$_2$NH + NH$_2$ ⟶ H$_2$CN + NH$_3$, CH$_2$NH + OH ⟶ H$_2$CN + H$_2$O and with V20 thermochemical data for H$_2$CN, HCNH and HCN (dotted lines).
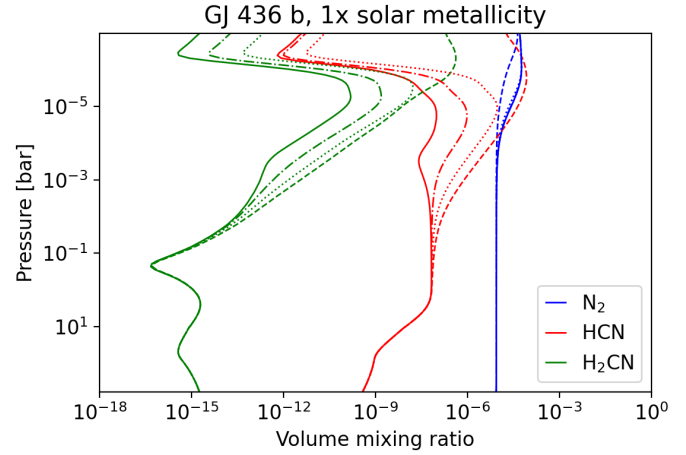
GJ 436 b, 1x solar metallicity

Fig. 14. Sensitivity analysis of the pre-exponential factor A of the reaction H$_2$CN + H ⟶ CH$_2$NH. Abundances profiles are calculated with the full V23 network (solid lines), with A divided by 10 (dashdot lines), with A divided by 100 (dotted lines) and without this reaction (dashed lines).

no visible difference with V23 was observed. We disabled the reaction CH$_2$NH + H ⟶ H$_2$CN + H$_2$, but other reactions such as CH$_2$NH + CH$_3$ ⟶ H$_2$CN + CH$_4$ and CH$_2$NH + NH$_2$ ⟶ H$_2$CN + NH$_3$ would replace its function in the HCN formation pathway, leading to smaller but very significant differences. Thus, we disabled all the H-abstraction reactions of CH$_2$NH in addition to the reaction H$_2$CN + H ⟶ CH$_2$NH, and found almost the same profile as V20. As disabling these reactions without disabling the reaction H$_2$CN + H ⟶ CH$_2$NH almost does not alter the V23 abundance profile, both of these reactions seem to be required to explain the differences between V23 and V20. The remaining difference was mainly located under 100 bar, where HCN and H$_2$CN abundances approach chemical equilibrium. Because the thermochemical data for V23 are different from V20 (Fig. D.1), we ran V23 with V20 thermochemical data for H$_2$CN, HCNH and HCN, and found a perfect match in this pressure range. Thus, we conclude that the differences between V23 and V20 observed in HCN abundance profiles for GJ 436 b at 1× solar metallicity are caused by the addition of the species CH$_2$NH to the network. The upper atmosphere differences are caused by the reaction H$_2$CN + H ⟶ CH$_2$NH, and the lower atmosphere differences are caused mainly by CH$_2$NH + H ⟶ H$_2$CN + H$_2$, but also to a lower extent by others H-abstraction reactions of CH$_2$NH with CH$_3$, NH$_2$ or OH.

Because of the importance of the reaction H$_2$CN + H ⟶ CH$_2$NH in these simulations and the large uncertainty in its reaction parameters (discussed in Sect. 2.8), we investigated its impact on the simulations with a sensitivity analysis. Figure 14 shows a sensitivity analysis on the pre-exponential factor A of this reaction. Multiple simulations were run with different pre-exponential factors for this reaction, up to a division factor of 100. Significant differences in HCN abundance of up to two orders of magnitude are found between values of A and of A/100, especially around 10^{-5} bar. At lower pressures however, the abundance is shown to be quite insensitive to changes in A, showing that the presence of the reaction remains impactful even with low estimates for this pre-exponential factor.

Given this complete shift in the major N-bearing species above 10^{-5} bar, we could expect CH$_2$NH abundance to be quite high. However, as shown in Fig. 15, the CH$_2$NH abundance profile remains two to four orders of magnitude lower than HCN

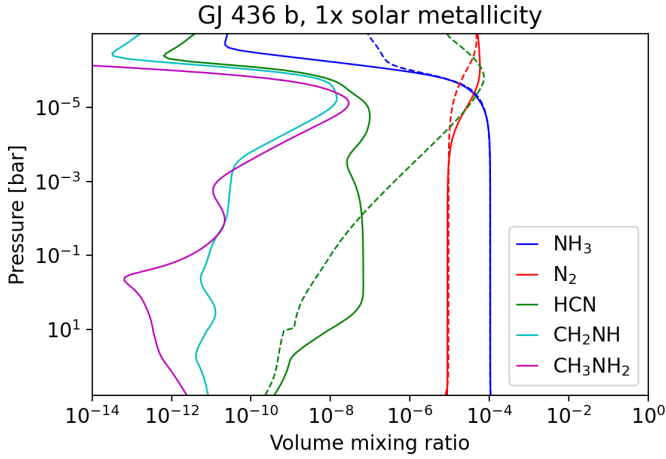## GJ 436 b, 1x solar metallicity

Fig. 15. Abundance profiles of CH_2NH and CH_3NH_2 compared with major N-bearing species for GJ 436 b with solar metallicity in V20 (dashed lines) and V23 (solid lines). CH_2NH and CH_3NH_2 are not included in V20.
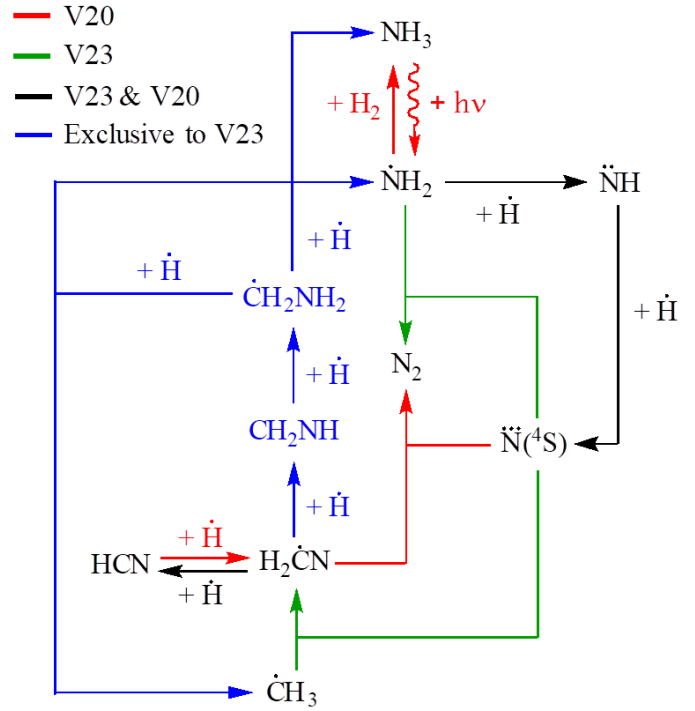

Fig. 16. HCN formation mechanism in V23 around 10^{-5} bar. The blue path is exclusive to V23 and absent from V20. The red reactions are dominant in V20 for the production of the species and minor but included in V23. The green reactions are dominant in V23 and minor but included in V20. The black reactions are dominant in both networks.
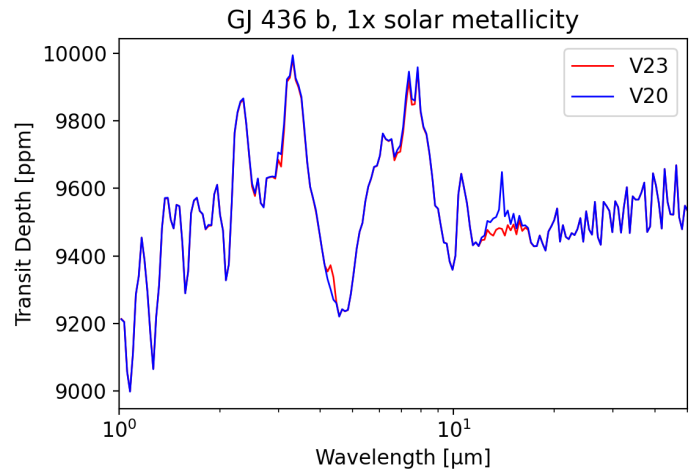
GJ 436 b, 1x solar metallicity

Fig. 17. Synthetic transmission spectra of GJ 436 b with a solar metallicity, at a resolution of 50, corresponding to the atmospheric compositions calculated with V23 (in red) and V20 (in blue).

abundance for pressures higher than 10^{-4} bar, and stays similar around 10^{-5} bar. For the N_2 abundance profile, we can see that its abundance increases with V23 in comparison to V20 around 10^{-5} bar, as this species becomes the main N-bearing species instead of HCN. The species CH_3NH_2 is also plotted, as we could expect the CH_2NH double bond to be saturated by H_2 and H atoms, but the main reaction producing CH_3NH_2 is the reaction $CH_3 + NH_2 \longrightarrow CH_3NH_2$. This reaction uses a PLOG description between 0.1 and 10 bar, hence its contribution for very low pressures is likely to be heavily overestimated. However, a detailed treatment of its pressure dependence raises the same problems as the reaction $H_2CN + H \longrightarrow CH_2NH$ because it is a barrierless, pressure dependent reaction. Therefore, we conclude that CH_2NH is an intermediate species that links HCN and N_2 abundances. The full mechanism linking these two species around 10^{-5} is detailed in Fig. 16. CH_2NH is mainly hydrogenated through the reaction $CH_2NH + H \longrightarrow CH_2NH_2$. The CH_2NH_2 radical then gets its C-N bond broken by the addition of another H atom through the reaction $CH_2NH_2 + H \longrightarrow CH_3 + NH_2$. These two reactions and the species CH_2NH and CH_2NH_2 are only included in V23 and not in V20. The NH_2 radical formed then gets destroyed by $N(^4S)$ atoms through the reaction $NH_2 + N(^4S) \longrightarrow N_2 + H + H$. This reaction has the same parameters between V23 and V20, although it is reversible in V20 and not in V23. Despite being reversible, the enthalpy difference between the reactants and the products is too high for it to be significantly reversed in V20. This is important because this reaction is an implicit combination of two other reactions, $NH_2 + N(^4S) \longrightarrow NNH + H$ and $NNH \longrightarrow N_2 + H$, and reversing the resulting combination $NH_2 + N(^4S) \longrightarrow N_2 + H + H$ would be unphysical. In addition, $N(^4S)$ atoms are produced from NH_2 through the reactions $NH_2 + H \longrightarrow NH + H_2$ and $NH + H \longrightarrow N(^4S) + H_2$. While the parameters for this second reaction are really similar between V20 and V23, for the first one, they are very different. Both consider this reaction as $NH + H_2 \longrightarrow NH_2 + H$ and use a temperature exponent of zero, but in V20 the activation energy is close to 20 kcal mol^{-1} while it is close to 15 kcal mol^{-1} in V23. The pre-exponential factor is also different, with a value of 10^{14} cm^3 mol^{-1} s^{-1} in V20 and 2.1×10^{13} cm^3 mol^{-1} s^{-1} in V23, 5 times lower. The

reaction $H_2CN + N(^4S) \longrightarrow N_2 + {}^3CH_2$, which is the main formation reaction of N_2 in V20 has similar parameters between V20 and V23, although they differ on the pre-exponential factor by a factor of 3.

3.2.3. Consequences on transmission spectra

These differences in the abundance profiles are also expressed in the synthetic transmission spectra showed in Fig. 17.
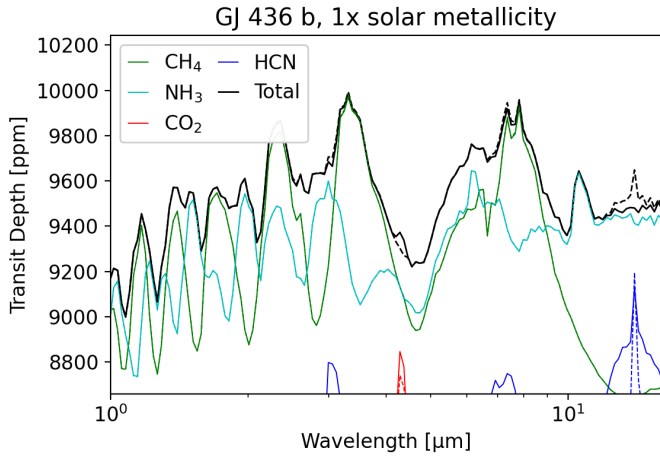
Fig. 18. Contributions of major species to the total synthetic transmission spectra of GJ 436 b with a solar metallicity and $K_{zz} = 10^9$ cm^2 s^{-1}. Dashed lines are for V20, while solid lines are for V23. In the middle, we see the CO_2 contribution that leads to a new feature in the spectrum with V23.
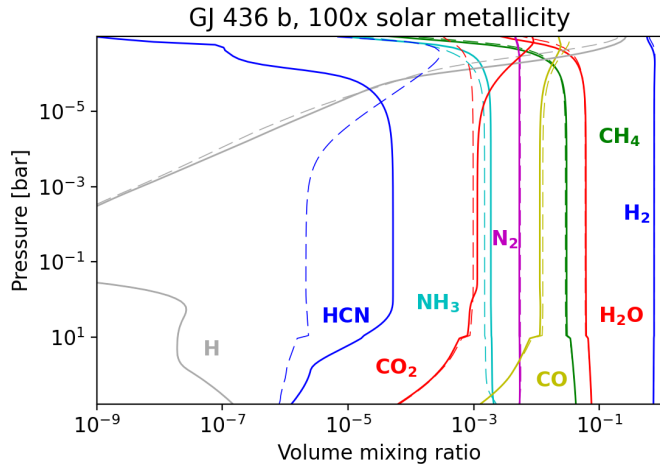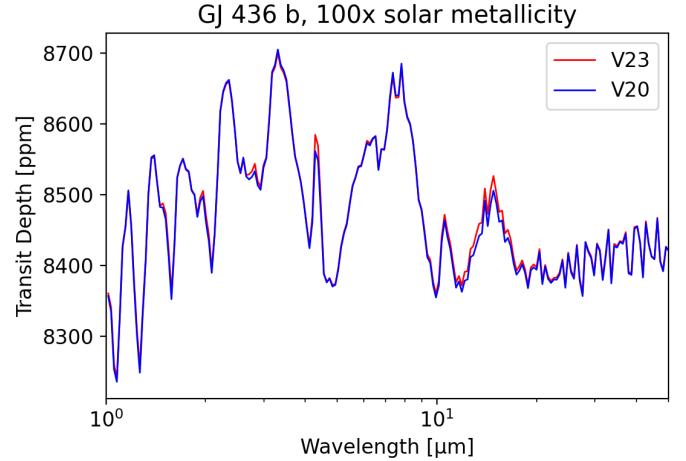

Fig. 20. Synthetic transmission spectra of GJ 436 b with 100 times solar metallicity, at a resolution of 50, corresponding to the atmospheric compositions calculated with V23 (in red) and V20 (in blue).

Fig. 19. Abundance profiles of GJ 436 b for 100 times solar metallicity and a constant eddy diffusion coefficient of 10^9 cm^2 s^{-1}. Dashed lines are for V20, while solid lines are for V23.

The higher CO_2 abundance obtained with V23 in the upper atmosphere increases the apparent radius of GJ 436 b around 4.2 μm, leading to the apparition of a new CO_2 feature with an amplitude of about 100 ppm. This happens because the transmission spectrum contribution of CO_2 approaches that of CH_4 and NH_3, which dominate at this wavelength for the abundance predicted with V20 (Fig. 18). Another major change in the spectrum is the disappearance of the HCN feature around 13 μm compared to an amplitude of about 200 ppm with V20, due to the drop in its abundance.

3.2.4. Case of 100 times solar metallicity

We also simulated the atmosphere of GJ 436 b assuming a higher metallicity (100× solar; 10^9 cm^2 s^{-1}), but keeping the same PT profile. In this case, variations between V20 and V23 are also observed, but to a lower extent (Fig. 19). Compared to the previous case with solar metallicity, the amplitude of HCN differences is lower, because the profile is strongly quenched, due to the higher abundance of related species that causes a higher flux of species. However, for pressures from 10 to 10^{-5} bar, HCN

abundance in V23 is still almost two orders of magnitude above that of V20. For pressures around 10^{-6} bar, the HCN abundance in V20 is almost four orders of magnitude greater than in V23. These changes directly relate to the network differences discussed for the solar metallicity case in Sect. 3.2.2, and particularly the reaction $H_2CN + H \longrightarrow CH_2NH$ for the upper atmosphere differences, and the reaction $CH_2NH + H \longrightarrow H_2CN + H_2$ for the lower atmosphere. We also observe differences in the thermochemical equilibrium region, which are due to discussed differences in the thermochemical data. This was verified through the same method described earlier, by disabling these specific reactions to see how they impact HCN abundance profile. In addition, CO_2 is more abundant in V23 than in V20 around 10^{-6} bar by almost one order of magnitude, due to differences in the $CO + OH \longrightarrow CO_2 + H$ reaction rates (Sect. 3.2.1). NH_3 abundance profile is also slightly higher in V23 than V20, because the quenching point seems to happen at slightly higher pressures. For this metallicity case, these variations in abundances have very little impact on the transmission spectrum (Fig. 20). The slight change in NH_3 abundance profiles barely causes some features to undergo an amplitude change, but HCN clearly does not show any impact on the spectrum, because its contribution is well under the contributions of CH_4 and NH_3 (Fig. E.1).

3.3. Case of GJ 1214 b

For network comparisons with the warm Neptune GJ 1214 b, we used a pressure dependent eddy diffusion coefficient profile calculated with the formula $K_{zz} = 3 \times 10^7 \times P^{-0.4}$ cm^2 s^{-1} given in Charnay et al. (2015). As this planet is expected to have a high metallicity (Désert et al. 2011; Bean et al. 2011; Gao et al. 2023; Kempton et al. 2023), we chose to model this planet with 100 times solar metallicity. The PT profile was taken from Venot et al. (2020) and the UV flux used was that of GJ 436. The resulting abundance profiles (Fig. 21) do not show a lot of difference between the two chemical networks. HCN abundance profile is still above the value predicted by V20 up to a factor of 100 around 1 bar, while other species are mildly affected, except for very low pressure regions around 10^{-6} bar, which are one order of magnitude above for CO and CO_2. Contrary to the previous cases of GJ 1214 b at 1× and 100× solar metallicity, the HCN abundance profile of V23 is never lower than that of V20, expect
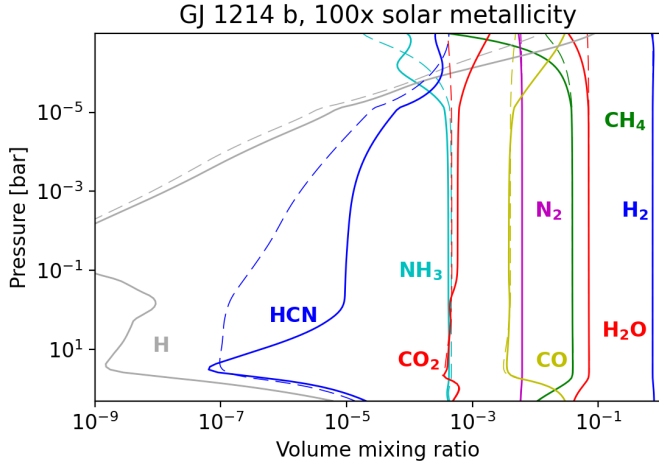
Fig. 21. Abundance profiles of GJ 1214 b for 100 times solar metallicity and a pressure-dependent eddy diffusion coefficient. Dashed lines are for V20, while solid lines are for V23.
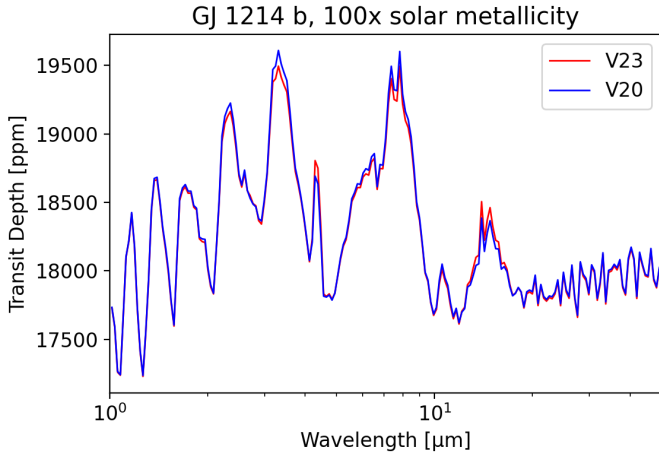

Fig. 23. Abundance profiles of HD 189733 b for solar metallicity and a pressure-dependent eddy diffusion coefficient. Dashed lines are for V20, while solid lines are for V23.

Fig. 22. Synthetic transmission spectra of GJ 1214 b, at a resolution of 50, corresponding to the atmospheric compositions calculated with V23 (in red) and V20 (in blue).

Fig. 24. Abundance profiles of HD 209458 b for solar metallicity and a pressure-dependent eddy diffusion coefficient. Dashed lines are for V20, while solid lines are for V23.

at the very limit of the P–T profile, around 10^{-7} bar. This means that the reaction $H_2CN + H \longrightarrow CH_2NH$ has very little impact on HCN in the upper atmosphere of this planet, and it was indeed verified by disabling the reaction. Similarly to previous cases and with the same method, for the remaining differences in the lower atmosphere, we identified the same responsible reactions to be $H_2CN + H \longrightarrow CH_2NH$, $CH_2NH + H \longrightarrow H_2CN + H_2$ and the related reactions previously discussed in Sect. 3.2.2. For the CO_2 abundance profile, the differences stem from the reaction $CO + OH \longrightarrow CO_2 + H$, as discussed in Sect. 3.2.1. The CO differences come from the reaction $C + OH \longrightarrow CO + H$, which is the only major production reaction at those pressures in V23. This reaction is also included in V20 with the same parameters. Then, CH_4 and H_2O follow the opposite trend, resulting (respectively) from a higher loss contribution of the reaction $CH_4 + CH \longrightarrow C_2H_4 + H$ and the reaction $H_2O + CH \longrightarrow H_2CO + H$ which is exclusive to V23.

Due to the low amplitude of these changes, the corresponding synthetic spectra (Fig. 22) shows no new features, with only a few minor variations in the amplitude of existing features, largely under observable values.
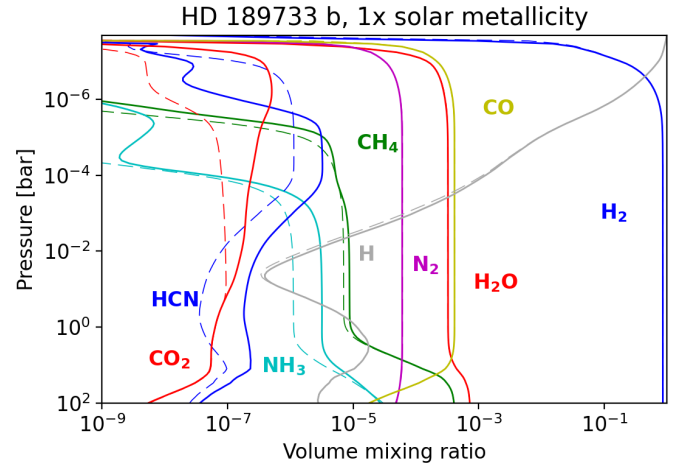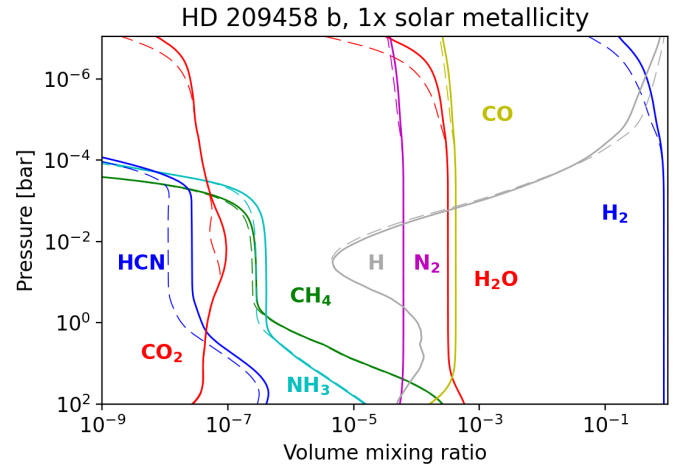
3.4. Case of HD 189733 b and HD 209458 b

While we observe that for warm Neptunes the most significant impacts of our new chemical scheme are found for low metallicity atmospheres, we examined the effect on two hot Jupiters: HD 189733 b and HD 209458 b. We used the same P–T profiles, UV fluxes, eddy diffusion coefficients, and metallicities as in Venot et al. (2020). The abundances profiles obtained using the two chemical schemes V20 and V23 are shown in Figs. 23 and 24.

For HD 189733 b, the only differences are for species lower than 10^{-5} abundance. CO_2 is more abundant in V23 around 10^{-6} bar than in V20, due to the $CO + OH \longrightarrow CO_2 + H$ reaction (Sect. 3.2.1). The abundances of NH_3 and HCN are slightly less than one order of magnitude higher in V23 than in V20 between 10 and 10^{-3} bar. The larger NH_3 difference between 10^{-4} and 10^{-6} bar is due to the reaction $CH_2NH_2 + H \longrightarrow {}^1CH_2 + NH_3$ which is analogous to the reaction $CH_2NH_2 + H \longrightarrow CH_3 + NH_2$ discussed in Sect. 3.2.2. The differences between 10 and 10^{-3} bar are explained by two reactions : $NH_3 + NH_2 \longrightarrow N_2H_3 + H_2$ and $NH_2 + NH_2 \longrightarrow N_2H_2 + H_2$. The first one is

not included in V23, while in V20 it contributes to NH_3 consumption. The second one is included in both networks, but the parameters used in the reactions are different, especially for the activation energy, which is 10 kcal mol^{-1} higher in V23 than in V20. When combined with the changes in the thermochemical data, the differences in these rate constants explain the differences between the HCN abundance profiles for pressures higher than 10^{-5} bar. For lower pressures, the reaction $H_2CN + H \longrightarrow CH_2NH$ increases HCN consumption in V23 in comparison to V20 as previously discussed, leading to over one order of magnitude less HCN in V23 than in V20. A very detailed comparison between the chemical schemes of Venot et al. (2012) and Moses et al. (2011) (which we name V12 and M11 in the following, respectively) has been performed by Moses (2014), taking HD 189733 b as a case study, with the parameters used in Venot et al. (2012). Thus, it is interesting to evaluate how the results obtained with our new scheme compare with these two schemes. The highlighted differences concerned the species NH_3, CH_4, and HCN.

With M11, NH_3 was one order of magnitude above V12 in the range 10 to 10^{-3} bar and one order of magnitude under V12 in the range 10^{-5} to 10^{-7} bar. The V23 NH_3 abundance profile halves this gap between M11 and V12 in the range 10 to 10^{-3} bar, being nearly half an order of magnitude above V12 and half an order of magnitude under M11. However, in the pressure range 10^{-5} to 10^{-7} bar, the V23 NH_3 abundance is much higher than in both chemical networks, reaching a difference of seven orders of magnitude around 10^{-5} bar.

For CH_4, the differences mainly concerned the pressure range 1 to 10^{-3} bar, with the M11 profiles being around half an order of magnitude above V12. The corresponding V23 profile slightly approaches the M11 profiles, also halving the gap between M11 and V12 for CH_4.

For HCN, the differences concerned the range 100 to 10^{-7} bar, the M11 profile being an order of magnitude above V12. The V23 profile comes closer to the M11 profile in comparison to both V12 and V20 for the range 100–10^{-5} bar, but the HCN abundance drops for V23 around 10^{-6} bar, resulting in a difference of three orders of magnitude with M11 at this pressure.

Overall, these results bring the abundances a bit closer to M11, but enhances differences in the upper atmosphere where new CH_2NH chemical pathways begin to take effect.

We calculated the synthetic transmission spectrum corresponding to the abundances obtained with V23 and V20 and observed some differences (see Fig. 25). The main effect is an increase of the transit depth between 10 and 20 μm, with an amplitude of up to 50 ppm. No new feature is created in the spectrum, but the differences generated are above the instrumental precision. Thus, the change of chemical scheme could impact the interpretations of the transmission spectrum and the retrieval of NH_3 abundance.

For the hotter HD 209458 b, the differences are even smaller than what we observed for HD 189733b, with an amplitude lower than one order of magnitude. The NH_3 and HCN abundances are still a bit higher in V23 as with all previous exoplanets, except for GJ 436 b with a solar metallicity. The reactions causing these differences are the same as for the case of HD 189733 b. Another minor difference is that CO_2, H_2O and H_2 are more abundant in V23 for pressures lower than 10^{-6} bar, unlike H atoms. The formation pathways of these species at this pressure being the same in V20 and V23, the differences must come from slight differences in the parameters of the reactions.
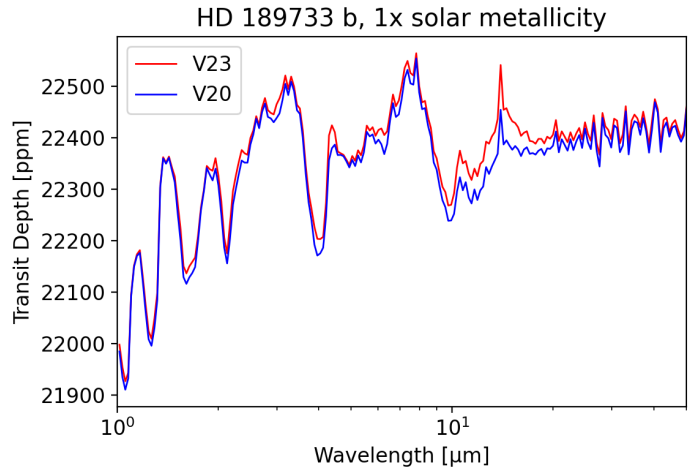

Fig. 25. Synthetic transmission spectra of HD 189733 b, at a resolution of 50, corresponding to the atmospheric compositions calculated with V23 (in red) and V20 (in blue).
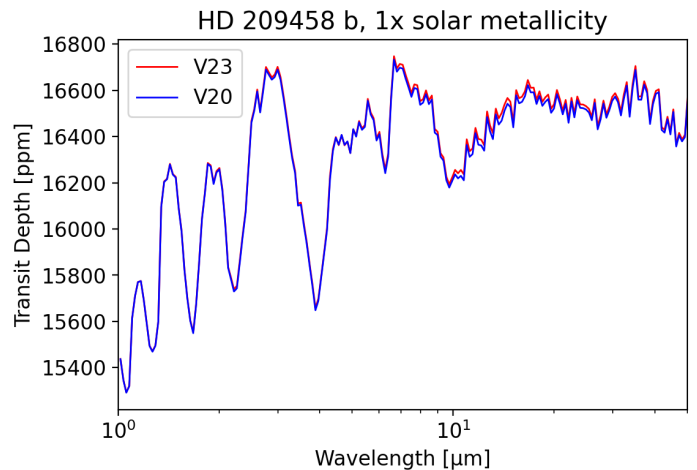

Fig. 26. Synthetic transmission spectra of HD 209458 b, at a resolution of 50, corresponding to the atmospheric compositions calculated with V23 (in red) and V20 (in blue).

Overall, the variations of abundances observed with V23 for this planet in comparison to V20 are very small, and concern mainly species with low abundances ($<10^{-6}$). As a consequence, the synthetic transmission spectra calculated for both networks (Fig. 26) are very similar.

4. Conclusion

In this work, we developed a new C_2 C/H/O/N detailed chemical scheme to model exoplanet disequilibrium chemistry. It was derived from experimentally tested combustion networks, extensively validated on 1618 experimental measurements on a wide range of conditions and compared to other chemical networks performances, such as V20 through a statistical study. Verifications, additions, and detailing of possibly missing radical reactions were also performed, resulting in a much more reliable network than Venot 2020. This network was then used to model two warm Neptunes and two hot Jupiters using the kinetic model FRECKLL, and the results were compared to those obtained with our previous chemical scheme, V20.

The chemistry differences were analyzed and new chemical pathways were found, such as the importance of CH_2NH and its formation through H_2CN to couple the nitrogen chemistry to CH_3 radicals. This effect has been highlighted in a solar metallicity warm Neptune, and is such expected to mainly impact warm exoplanets with a low metallicity. Transmission spectra were also simulated using TauREx 3.1 and the resulting changes in abundances were found to significantly impact the spectrum for GJ 436 b, with differences around 100 ppm for CO_2 at 4.2 μm and 200 ppm for HCN at 13 μm. The amplitude of these features is within the detection capabilities of JWST, which confirms that disequilibrium chemistry model accuracy is crucial to draw correct conclusions from observations. In the context of ongoing and future missions (e.g., JWST and Ariel), disequilibrium chemistry modelling will become increasingly important as we get access to higher precision observations. Improvements are still awaited in the development of experimentally validated sulfur chemical scheme: a compound such as SO_2 has been recently been detected with the JWST and is typically a product of photochemistry (Tsai et al. 2022). Expanding our network to sulfur species and their coupling to carbon and nitrogen species will be the next step toward a more complete chemical scheme addressing modern problematics in the exoplanet chemistry field. More in-depth insights on the critical reactions for each species through sensitivity analysis or other methods in a wide range of exoplanetary conditions could also help to further improve the reliability of these networks, enabling to identify the key reactions in the mechanism and could help to focus the community's efforts and reduce the associated uncertainty through more accurate but computationally intensive ab initio calculations such as VRC-TST for barrierless reactions and RRKM/ME for pressure dependence. As in situ experimentation with probes is impossible in the field of exoplanet chemistry, the use of chemical networks validated on combustion experiments remains the only way to validate our kinetic models to this day.

References

Allen, M. T., Yetter, R. A., & Dryer, F. L. 1998, Combust. Flame, 112, 302

Al-Refaie, A. F., Changeat, Q., Waldmann, I. P., & Tinetti, G. 2021, ApJ, 917, 37

Al-Refaie, A. F., Changeat, Q., Venot, O., Waldmann, I. P., & Tinetti, G. 2022a, ApJ, 932, 123

Al-Refaie, A. F., Venot, O., Changeat, Q., & Edwards, B. 2022b, ArXiv e-prints [arXiv:2209.11203]

Aronowitz, D., Santoro, R., Dryer, F., & Glassman, I. 1979, Symp. (Int.) Combust., 17, 633

Au, J. W., & Brion, C. E. 1997, Chem. Phys., 218, 109

Au, J. W., Cooper, G., Burton, G. R., Olney, T. N., & Brion, C. E. 1993, Chem. Phys., 173, 209

Battin-Leclerc, F., Blurock, E., Bounaceur, R., et al. 2011, Chem. Soc. Rev., 40, 4762

Bauerle, S., Klatt, M., & Wagner, H. 1995, Phys. Chem. Chem. Phys., 99, 870

Baulch, D., Cobos, C., Cox, R., et al. 1994, J. Phys. Chem. Ref. Data, 23, 847

Bean, J. L., Désert, J.-M., Kabath, P., et al. 2011, ApJ, 743, 92

Biehl, H., & Stuhl, F. 1991, J. Photochem. Photobiol. A: Chem., 59, 135

Bounaceur, R., Herbinet, O., Fournet, R., et al. 2010, in SAE 2010 World Congress & Exhibition, 2010-01-0546

Bounaceur, R., Glaude, P.-A., Sirjean, B., et al. 2015, J. Eng. Gas Turbines Power, 138, 021505

Brion, C. E., Tan, K. H., van der Wiel, M. J., & van der Leeuw, P. E. 1979, in Physics of Electronic and Atomic Collisions: ICPEAC XI, eds. K. Takayanagi, & N. Oda, 52

Burke, U., Metcalfe, W. K., Burke, S. M., et al. 2016, Combust. Flame, 165, 125

Burkholder, J., Sander, S., Abbatt, J., et al. 2020, Chemical Kinetics and Photochemical Data for Use in Atmospheric Studies, evaluation number 19, Tech. rep. (Pasadena, CA: Jet Propulsion Laboratory, National Aeronautics and Space)

Burton, G. R., Chan, W. F., Cooper, G., & Biron, C. E. 1992, Chem. Phys., 167, 349

Burton, G. R., Chan, W. F., Cooper, G., & Brion, C. 1993, Chem. Phys., 177, 217

Cathonnet, M., Boettner, J. C., & James, H. 1982, J. Chim. Phys., 79, 475

Chan, W. F., Cooper, G., & Brion, C. E. 1992, Chem. Phys., 168, 375

Chan, W. F., Cooper, G., & Brion, C. 1993a, Chem. Phys., 170, 99

Chan, W. F., Cooper, G., & Brion, C. 1993b, Chem. Phys., 170, 111

Chan, W. F., Cooper, G., & Brion, C. E. 1993c, Chem. Phys., 178, 387

Chan, W. F., Cooper, G., Sodhi, R., & Brion, C. 1993d, Chem. Phys., 170, 81

Charnay, B., Meadows, V., & Leconte, J. 2015, ApJ, 813, 15

Chen, F., & Wu, C. R. 2004, J. Quant. Spectrosc. Rad. Transfer, 85, 195

Chen, F., Judge, D., Wu, C. R., & Caldwell, J. 1998, Planet. Space Sci., 47, 261

Cheng, B.-M., Bahou, M., Chen, W.-C., et al. 2002, J. Chem. Phys., 117, 1633

Cheng, B.-M., Lu, H.-C., Chen, H.-K., et al. 2006, ApJ, 647, 1535

Cooper, G., Burton, G. R., & Brion, C. 1995a, J. Electron Spectrosc. Relat. Phenom., 73, 139

Cooper, G., Olney, T. N., & Brion, C. 1995b, Chem. Phys., 194, 175

Cooper, G., Anderson, J. E., & Brion, C. E. 1996, Chem. Phys., 209, 61

Curran, H. J. 2019, Proc. Combust. Inst., 37, 57

Dagaut, P., Boettner, J.-C., & Cathonnet, M. 1990, Int. J. Chem. Kinet., 22, 641

Dagaut, P., Glarborg, P., & Alzueta, M. 2008a, Progr. Energy Combust. Sci., 34, 1

Dagaut, P., Glarborg, P., & Alzueta, M. U. 2008b, Progr. Energy Combust. Sci., 34, 1

Désert, J.-M., Bean, J., Miller-Ricci Kempton, E., et al. 2011, ApJ, 731, L40

Drummond, B., Hébrard, E., Mayne, N. J., et al. 2020, A&A, 636, A68

Fahr, A. 2003, J. Mol. Spectrosc., 217, 249

Fahr, A., Hassanzadeh, P., & Atkinson, D. B. 1998, Chem. Phys., 236, 43

Fally, S., Vandaele, A. C., Carleer, M., et al. 2000, J. Mol. Spectrosc., 204, 10

Fillion, J. H., Ruiz, J., Yang, X. F., et al. 2004, J. Chem. Phys., 120, 6531

Gao, P., Piette, A. A. A., Steinrueck, M. E., et al. 2023, ApJ, 951, 96

Georgievskii, Y., & Klippenstein, S. J. 2003a, J. Phys. Chem. A, 107, 9776

Georgievskii, Y., & Klippenstein, S. J. 2003b, J. Chem. Phys., 118, 5442

Giménez-López, J., Millera, A., Bilbao, R., & Alzueta, M. 2010, Combust. Flame, 157, 267

Glarborg, P., Miller, J., & Kee, R. 1986, Combust. Flame, 65, 177

Glarborg, P., Miller, J. A., Ruscic, B., & Klippenstein, S. J. 2018, Progr. Energy Combust. Sci., 67, 31

Gordon, I., Rothman, L., Hargreaves, R., et al. 2022, JQSRT, 277, 107949

Heays, A. N., Bosman, A. D., & van Dishoeck, E. F. 2017, A&A, 602, A105

Hébrard, E., Dobrijevic, M., Bénilan, Y., & Raulin, F. 2006, in 36th COSPAR Scientific Assembly, 36, 526

Hébrard, E., Dobrijevic, M., Loison, J. C., et al. 2013, A&A, 552, A132

Held, T., & Dryer, F. 1994, Symp. (Int.) Combust., 25, 901

Hochanadel, C. J., Sworski, T. J., & Ogren, P. J. 1980, J. Phys. Chem., 84, 231

Hubrich, C., & Stuhl, F. 1980, J. Photochem., 12, 93

Huebner, W. F., Keady, J. J., & Lyon, S. P. 1992, Ap&SS, 195, 1

Huestis, D. L., & Berkowitz, J. 2010, in AAS/Division for Planetary Sciences Meeting Abstracts, 42, 48.13

Huffman, R. E. 1969, Can. J. Chem., 47, 1823

Iida, Y., Carnovale, F., Daviel, S., & Brion, C. E. 1986, Chem. Phys., 105, 211

Joshi, A., & Wang, H. 2006, Int. J. Chem. Kinet., 38, 57

Kameta, K., Machida, S., Kitajima, M., et al. 1996, J. Electron Spectrosc. Relat. Phenom., 79, 391

Kameta, K., Kouchi, N., Ukai, M., & Hatano, Y. 2002, J. Electron Spectrosc. Relat. Phenom., 123, 225

Kee, R., Rupley, F., Miller, J., et al. 2006, Reaction Design, San Diego, CA, 115

Kempton, E. M.-R., Zhang, M., Bean, J. L., et al. 2023, Nature, 620, 67

Kéromnès, A., Metcalfe, W. K., Heufer, K. A., et al. 2013, Combust. Flame, 160, 995

Kim, T. J., Yetter, R. A., & Dryer, F. L. 1994, Symp. (Int.) Combust., 25, 759

Klippenstein, S. J. 1992, J. Chem. Phys., 96, 367

Konnov, A. 2009, Combust. Flame, 156, 2093

Konnov, A. A., Barnes, F. J., Bromly, J. H., Zhu, J. N., & Zhang, D.-k. 2005, Combust. Flame, 141, 191

Kruse, T., & Roth, P. 1997, J. Phys. Chem. A, 101, 2138

Laufer, A. H., & Keller, R. A. 1971, J. Am. Chem. Soc., 93, 61

Le Cong, T., & Dagaut, P. 2009, Energy Fuels, 23, 725

Lee, A. Y., Yung, Y. L., Cheng, B.-M., et al. 2001, ApJ, 551, L93

Li, J., Kazakov, A., & Dryer, F. L. 2001, Int. J. Chem. Kinetics, 33, 859

Limão-Vieira, P., Eden, S., Mason, N. J., & Hoffmann, S. V. 2003, Chem. Phys. Lett., 376, 737

Linsky, J. L., Fontenla, J., & France, K. 2013, ApJ, 780, 61

Lodders, K. 2010, Astrophys. Space Sci. Proc., 16, Principles and Perspectives in Cosmochemistry, 379

Loison, J.-C., Kable, S. H., Houston, P. L., & Burak, I. 1991, J. Chem. Phys., 94, 1796

Matthews, J., Sinha, A., & Francisco, J. S. 2005, J. Chem. Phys., 122, 221101

Meller, R., & Moortgat, G. K. 2000, J. Geophys. Res., 105, 7089

Menou, K. 2022, MNRAS, 517, 2714

Moses, J. I. 2014, Philos. Trans. Roy. Soc. A Math. Phys. Eng. Sci., 372

Moses, J. I., Visscher, C., Fortney, J. J., et al. 2011, ApJ, 737, 15

Mota, R., Parafita, R., Giuliani, A., et al. 2005, Chem. Phys. Lett., 416, 152

Mueller, M. A., Kim, T. J., Yetter, R. A., & Dryer, F. L. 1999, Int. J. Chem. Kinet., 31, 113

Nativel, D., Shu, B., Herzler, J., Fikri, M., & Schulz, C. 2019, Proc. Combust. Inst., 37, 197

Nizamov, B., & Dagdigian, P. J. 2003, J. Phys. Chem. A, 107, 2256

Norton, T. S., & Dryer, F. L. 1989, Combust. Sci. Tech., 63, 107

Nuth, J. A., & Glicker, S. 1982, JQSRT, 28, 223

Olney, T. N., Cann, N. M., Cooper, G., & Brion, C. E. 1997, Chem. Phys., 223, 59

Orkin, V. L., Huie, R. E., & Kurylo, M. J. 1997, J. Phys. Chem. A, 101, 9118

Orphal, J., & Chance, K. 2003, J. Quant. Spec. Radiat. Transf., 82, 491

Peng, Z., Carrasco, N., & Pernot, P. 2014, GeoResJ, 1, 33

Ranjan, S., Schwieterman, E. W., Harman, C., et al. 2020, ApJ, 896, 148

Ren, W., Dames, E., Hyland, D., Davidson, D. F., & Hanson, R. K. 2013, Combust. Flame, 160, 2669

Rimmer, P. B., & Helling, C. 2016, ApJS, 224, 9

Rotzoll, G. 1985, J. Anal. Appl. Pyrolysis, 9, 43

Roudier, G. M., Swain, M. R., Gudipati, M. S., et al. 2021, AJ, 162, 37

Samson, J. A., & Cairns, R. 1964, J. Geophys. Res., 69, 4583

Samson, J. A. R., & Haddad, G. N. 1994, J. Opt. Soc. Am. B Opt. Phys., 11, 277

Sander, S. P. 1986, J. Phys. Chem., 90, 4135

Senosiain, J., Klippenstein, S., & Miller, J. 2005, Proc. Combust. Inst., 30, 945

Stark, G., Smith, P. L., Huber, K. P., et al. 1992, J. Chem. Phys., 97, 4809

Stark, G., Yoshino, K., Smith, P., & Ito, K. 2007, JQSRT, 103, 67

Stevenson, K. B., Harrington, J., Nymeyer, S., et al. 2010, Nature, 464, 1161

Tennyson, J., & Yurchenko, S. N. 2012, MNRAS, 425, 21

Teslja, A., Dagdigian, P. J., Banck, M., & Eisfeld, W. 2006, J. Phys. Chem. A, 110, 7826

Tsai, S.-M., Lyons, J. R., Grosheintz, L., et al. 2017, ApJS, 228, 20

Tsai, S.-M., Malik, M., Kitzmann, D., et al. 2021, ApJ, 923, 264

Tsai, S.-M., Lee, E. K. H., Powell, D., et al. 2023, Nature, 617, 483

Tsang, W., & Hampson, R. 1986, J. Phys. Chem. Reference Data, 15, 1087

Vaghjiani, G. L. 1993, J. Chem. Phys., 98, 2123

Vaghjiani, G. L., & Ravishankara, A. R. 1989, J. Geophys. Res., 94, 3487

Vandaele, A. C., Hermans, C., Fally, S., et al. 2002, J. Geophys. Res. (Atmos.), 107, 4348

Venot, O., Hébrard, E., Agúndez, M., et al. 2012, A&A, 546, A43

Venot, O., Hébrard, E., Agúndez, M., Decin, L., & Bounaceur, R. 2015, A&A, 577, A33

Venot, O., Bénilan, Y., Fray, N., et al. 2018, A&A, 609, A34

Venot, O., Cavalié, T., Bounaceur, R., et al. 2020, A&A, 634, A78

Wakelam, V., Herbst, E., Loison, J.-C., et al. 2012, ApJS, 199, 21

Wang, H., & Sheen, D. A. 2015, Progr. Energy Combust. Sci., 47, 1

Warth, V., Battin-Leclerc, F., Fournet, R., et al. 2000, Comput. Chem., 24, 541

Wu, C. Y. R., Chen, F. Z., & Judge, D. L. 2001, J. Geophys. Res.: Planets, 106, 7629

Wu, C. Y. R., Chen, F. Z., & Judge, D. L. 2004, J. Geophys. Res.: Planets, 109, E07S15

Wu, Y., Panigrahy, S., Sahu, A. B., et al. 2021, Combust. Flame, 226, 229

Yokelson, R., Burkholder, J. B., Fox, R., Talukdar, R. K., & Ravishankara, A. 1994, J. Phys. Chem., 98, 13144

Yoshino, K., Parkinson, W. H., Ito, K., & Matsui, T. 2005, J. Mol. Spectrosc., 229, 238

Zamyatina, M., Hébrard, E., Drummond, B., et al. 2023, MNRAS, 519, 3129

Zhou, C.-W., Li, Y., Burke, U., et al. 2018, Combust. Flame, 197, 423

Appendix A: Experimental data

Table A.1: Experimental conditions used for comparison and simulation with each C/H/O/N mechanism.

N°	N_{points}	Reaction conditions	Measured quantity	Variable	Temperature (K)	Pressure (bar)	Reaction time (s)
1	15	CH_3OH Combustion	IDT	Temperature	1000 - 1500	10.18, 49.18	N/A
2	33	CH_3OH Combustion	Mole Fraction	Time	823	0.26	26
3	112	CH_3OH Combustion	Mole Fraction	Time	949	2.5	0.5
4	99	CH_3OH Pyrolysis	Mole Fraction	Time	1266, 1368, 1458, 1567, 1610	2.5, 2.4, 2.3, 2.1, 2.2	0.0015
5	48	CH_3OH Combustion	Mole Fraction	Temperature	700 - 1200	20	1
6	54	CH_3OH Combustion	Mole Fraction	Time	1000	1	0.27
7	64	CH_3OH Combustion	Mole Fraction	Time	1031	1	0.125
8	68	CH_3OH Combustion	Mole Fraction	Time	783	15	3.5
9	72	CH_4 Combustion	Mole Fraction	Temperature	900 - 1200	10	1
10	24	H_2 Combustion	Mole Fraction	Temperature	800 - 1150	10	1
11	61	H_2 Combustion	Mole Fraction	Time	934	3.02	0.7
12	16	H_2 Combustion in CO	Mole Fraction	Temperature	850 - 1200	1	1
13	75	$CO + H_2O$	Mole Fraction	Time	1040	1, 2.4, 3.46, 6.5, 9.6	1.05
14	45	H_2 Combustion	IDT	Temperature	900 - 1700	1, 4, 16	N/A
15	72	HCN Combustion	Mole Fraction	Temperature	900 - 1500	1	195 / T
16	83	CH_4 Pyrolysis	Mole Fraction	Temperature	1250 - 1500	1	4550 / T
17	60	CH_4 Pyrolysis	Mole Fraction	Temperature	1600 - 2400, 1300 - 2000	1.5, 30	0.003, 0.015
18	56	Ethanol Pyrolysis	Mole Fraction	Temperature	1000 - 1300	0.74	0.006
19	399	Ethanol Pyrolysis	Mole Fraction	Time	950	3, 6, 9, 12	0.4, 0.8, 1.2, 1.4
20	87	$HCN + NO$ ($+ NH_3$) Combustion	Mole Fraction	Temperature	900 - 1500	1	197 / T
21	75	$H_2 + N_2O$	Mole Fraction	Time	995	3	0.5

N° is the condition reference number and N_{points} is the number of experimental measurements in the set.

Table A.1: (Continued). Species data refers to the species whose mole fraction has been measured.

N°	Reactor	Parameter study	Reactants	Species data	Data Source
1	Shock Tube	Pressure	5.7 % CH_3OH, 8.55 % O_2, Ar	N/A	Burke et al. (2016)
2	Static Reactor	N/A	5.89 % CH_3OH, 8.84 % O_2, N_2	H_2, CO, CO_2, CH_3OH and CH_2O	Cathonnet et al. (1982)
3	Plug Flow	N/A	0.333 % CH_3OH, 0.601 % O_2, N_2	CH_3OH, O_2, H_2O, CO, H_2 and CO_2	Held & Dryer (1994)
4	Shock Tube	N/A	1 % CH_3OH, Ar	CH_3OH, CO	Ren et al. (2013)
5	PSR	N/A	0.24 % CH_3OH, 0.3 % O_2, N_2	CH_3OH, O_2, CO and CO_2	Burke et al. (2016)
6	Plug Flow	N/A	0.735 % CH_3OH, 0.65 % O_2, N_2	CH_3OH, CH_2O, CO	Aronowitz et al. (1979)
7	Plug Flow	N/A	0.93 % CH_3OH, 1.18 % O_2, N_2	O_2, CH_3OH, CO, CO_2 and CH_2O	Norton & Dryer (1989)
8	Plug Flow	N/A	0.415 % CH_3OH, 0.6 % O_2, N_2	O_2, CH_3OH, CO and CH_2O	Held & Dryer (1994)
9	PSR	N/A	0.3 % CH_4, 0.00055 % C_2H_6, 1.2 % O_2, N_2	CO, CO_2, CH_4, C_2H_6, C_2H_4, C_2H_2	Dagaut et al. (1990)
10	PSR	N/A	0.93 % H_2, 5 % O_2, N_2	H_2, H_2O	Le Cong & Dagaut (2009)
11	Plug Flow	N/A	0.95 % H_2, 0.495 % O_2, N_2	H_2, O_2 and H_2O	Mueller et al. (1999)
12	PSR	N/A	0.2 % H_2, 0.2 % CO, 2 % O_2, N_2	H_2, CO_2	Le Cong & Dagaut (2009)
13	Plug Flow	Pressure	1 % CO, 0.65 % H_2O, 0.5 % O_2, N_2	CO	Kim et al. (1994)
14	Shock Tube	Pressure	0.81 % H_2, 4.03 % O_2, Ar	N/A	Kéromnès et al. (2013)
15	Plug Flow	Equivalence Ratio	0.1 % HCN, O_2, 0.7 % H_2O, 25 % Ar, CO_2	HCN, CO	Giménez-López et al. (2010)
16	Plug Flow	Mixtures	CH_4, CO_2, C_2H_6, N_2	CH_4, H_2, C_2H_2, C_2H_4, C_2H_6, CO, CO_2	Kéromnès et al. (2013)
17	Shock Tube	Pressure	10 % CH_4, 90 % Ar	CH_4, C_2H_2, C_2H_4	Nativel et al. (2019)
18	Plug Flow	N/A	2.8 % C_2H_5OH, 97.2 % Ar	C_2H_5OH, C_2H_4, CH_3CHO, H_2, CH_4	Rotzoll (1985)
19	Plug Flow	Pressure	0.3 % C_2H_5OH, 0.0035 % O_2, Ar	C_2H_5OH, H_2O, C_2H_4, CH_3CHO, CO, CH_2O, CH_4	Li et al. (2001)
20	Plug Flow	Mixtures	HCN, O_2, NO, H_2O, CO, NH_3	NO, CO, HCN, N_2O, NH_3	Dagaut et al. (2008b)
21	Plug Flow	N/A	0.53 % H_2, 1.1 % N_2O, N_2	N_2O, H_2O, H_2, NO, NH_3	Allen et al. (1998)

Appendix B: Photodissociation data

Table B.1: Photodissociation pathways, cross-sections, and quantum yields used in this study.

| Species	Products	Cross sections	Quantum yields
H_2O	$H + OH$	Chan et al. (1993c); Fillion et al. (2004);	Heays et al. (2017)
	$H_2 + O(^1D)$	Mota et al. (2005); Ranjan et al. (2020)	
	$H + H + O(^3P)$		
CO_2	$CO + O(^1D)$	Stark et al. (2007); Huestis & Berkowitz (2010);	Heays et al. (2017)
	$CO + O(^3P)$	Venot et al. (2018)	
H_2CO	$H_2 + CO$	Cooper et al. (1996); Meller & Moortgat (2000)	Heays et al. (2017)
	$H + HCO$		
	$H + H + CO$		
OH	$O(^1D) + H$	Huebner et al. (1992)	Heays et al. (2017)
	$O(^3P) + H$		
OOH	$OH + O(^3P)$	Heays et al. (2017)	
CO	$C + O(^3P)$	Olney et al. (1997)	Heays et al. (2017)
	$C + O(^1D)$		
H_2	$H + H$	Samson & Haddad (1994);	Heays et al. (2017)
		Chan et al. (1992); Olney et al. (1997)	
HCO	$H + CO$	Loison et al. (1991); Hochanadel et al. (1980)	
CH_3OH	$H_2CO + H_2$	Burton et al. (1992); Cheng et al. (2002)	Heays et al. (2017)
	$CH_3 + OH$		
CH_3OOH	$CH_3O + OH$	Vaghjiani & Ravishankara (1989); Matthews et al. (2005)	
CH_2CO	$^3CH_2 + CO$	Laufer & Keller (1971)	
CH_3CHO	$CH_4 + CO$	Limão-Vieira et al. (2003); Burkholder et al. (2020)	Heays et al. (2017)
	$CH_3 + HCO$		
CH_3	$^1CH_2 + H$	Heays et al. (2017)	Heays et al. (2017)
CH_4	$CH_3 + H$	Au et al. (1993); Lee et al. (2001);	Peng et al. (2014)
	$^1CH_2 + H_2$	Kameta et al. (2002); Chen & Wu (2004)	
	$^1CH_2 + H + H$		
	$^3CH_2 + H + H$		
	$CH + H_2 + H$		
C_2H	$C + C + H$	Heays et al. (2017); Fahr (2003)	
C_2H_2	$C_2H + H$	Cooper et al. (1995a); Wu et al. (2001)	Heays et al. (2017); Hébrard et al. (2013)
C_2H_3	$C_2H_2 + H$	Fahr et al. (1998)	
C_2H_4	$C_2H_2 + H_2$	Cooper et al. (1995b); Orkin et al. (1997);	Heays et al. (2017)
	$C_2H_2 + H + H$	Wu et al. (2004)	
C_2H_6	$C_2H_4 + H_2$	Au et al. (1993); Kameta et al. (1996);	Heays et al. (2017); Hébrard et al. (2006)
	$C_2H_4 + H + H$	Lee et al. (2001); Chen & Wu (2004)	
	$C_2H_2 + H_2 + H_2$		
	$CH_4 + {}^1CH_2$		
	$CH_3 + CH_3$		
N_2	$N(^2D) + N(^4S)$	Samson & Cairns (1964); Huffman (1969);	
		Stark et al. (1992); Chan et al. (1993d)	
NH_2	$NH + H$	Heays et al. (2017)	Heays et al. (2017)
NH_3	$NH_2 + H$	Burton et al. (1993); Chen et al. (1998);	Heays et al. (2017)
	$NH + H_2$	Cheng et al. (2006)	
	$NH + H + H$		
N_2H_4	$N_2H_3 + H$	Vaghjiani (1993); Biehl & Stuhl (1991)	
HCN, HNC	$CN + H$	Nuth & Glicker (1982); Bénilan et al. (in prep.);	Heays et al. (2017)
		Venot et al. (in prep.)	
H_2CN	$HCN + H$	Nizamov & Dagdigian (2003); Teslja et al. (2006)	
C_2N_2	$CN + CN$	Bénilan et al. (in prep.)	
NO	$N(^4S) + O(^3P)$	Iida et al. (1986); Chan et al. (1993b)	Heays et al. (2017)
NO_2	$NO + O(^3P)$	Au & Brion (1997); Vandaele et al. (2002)	Heays et al. (2017)
	$NO + O(^1D)$		
NO_3	$NO_2 + O(^3P)$	Orphal & Chance (2003); Sander (1986)	Heays et al. (2017)
	$NO + O_2$	Yokelson et al. (1994)	
HNO_2	$NO + OH$	Burkholder et al. (2020)	
HNO_3	$NO_2 + OH$	Burkholder et al. (2020)	
N_2O	$N_2 + O(^1D)$	Burkholder et al. (2020); Hubrich & Stuhl (1980)	Heays et al. (2017)
O_2	$O(^3P) + O(^3P)$	Brion et al. (1979); Yoshino et al. (2005)	Heays et al. (2017)
	$O(^1D) + O(^3P)$	Fally et al. (2000); Chan et al. (1993a)	
	$O(^1D) + O(^1D)$		
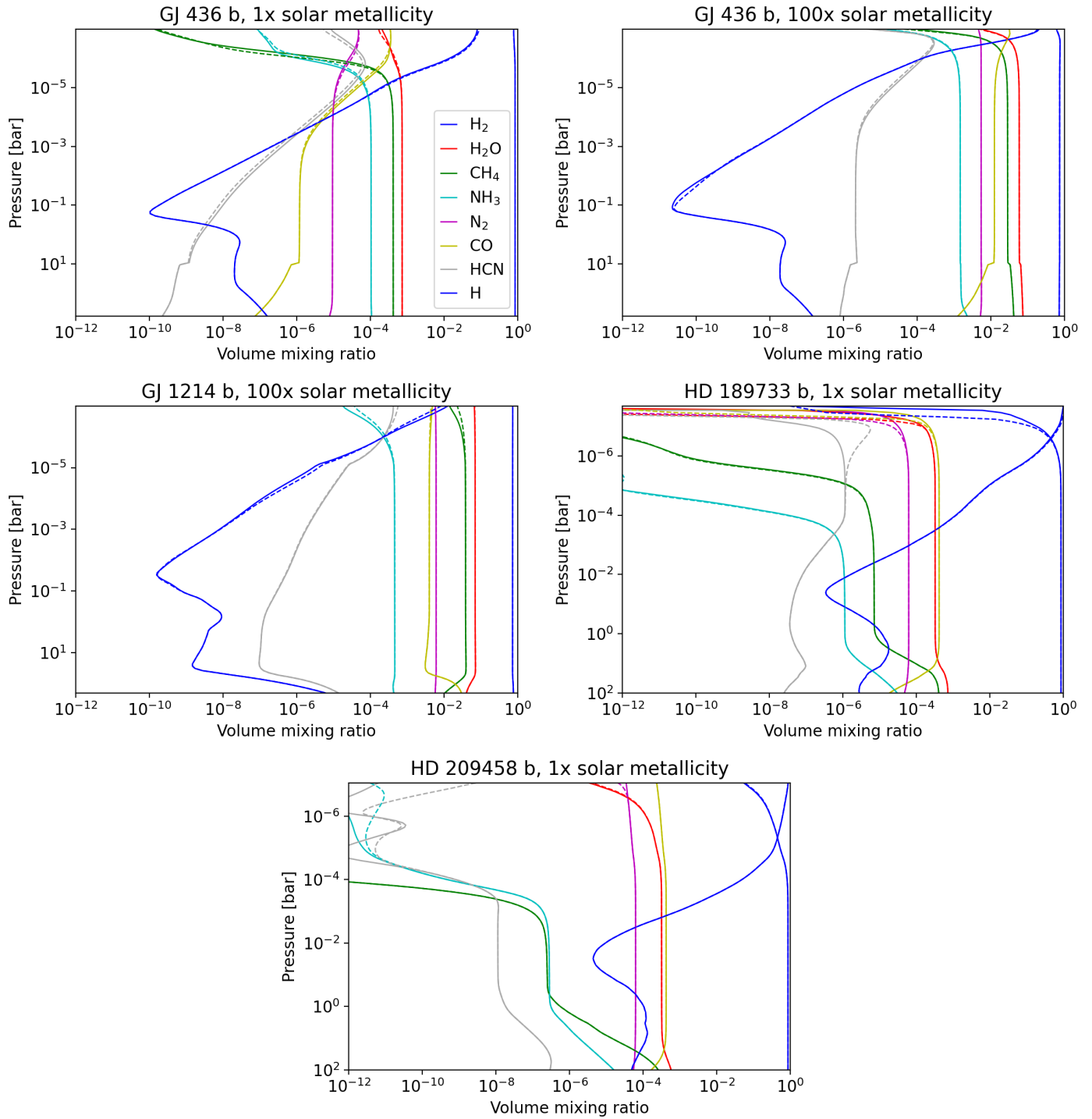
Fig. B.1. Abundance profiles of the main species for all exoplanet cases in Table 3, computed with V20. Dashed lines are abundances based on old photolysis data and solid lines are based on updated photolysis data.

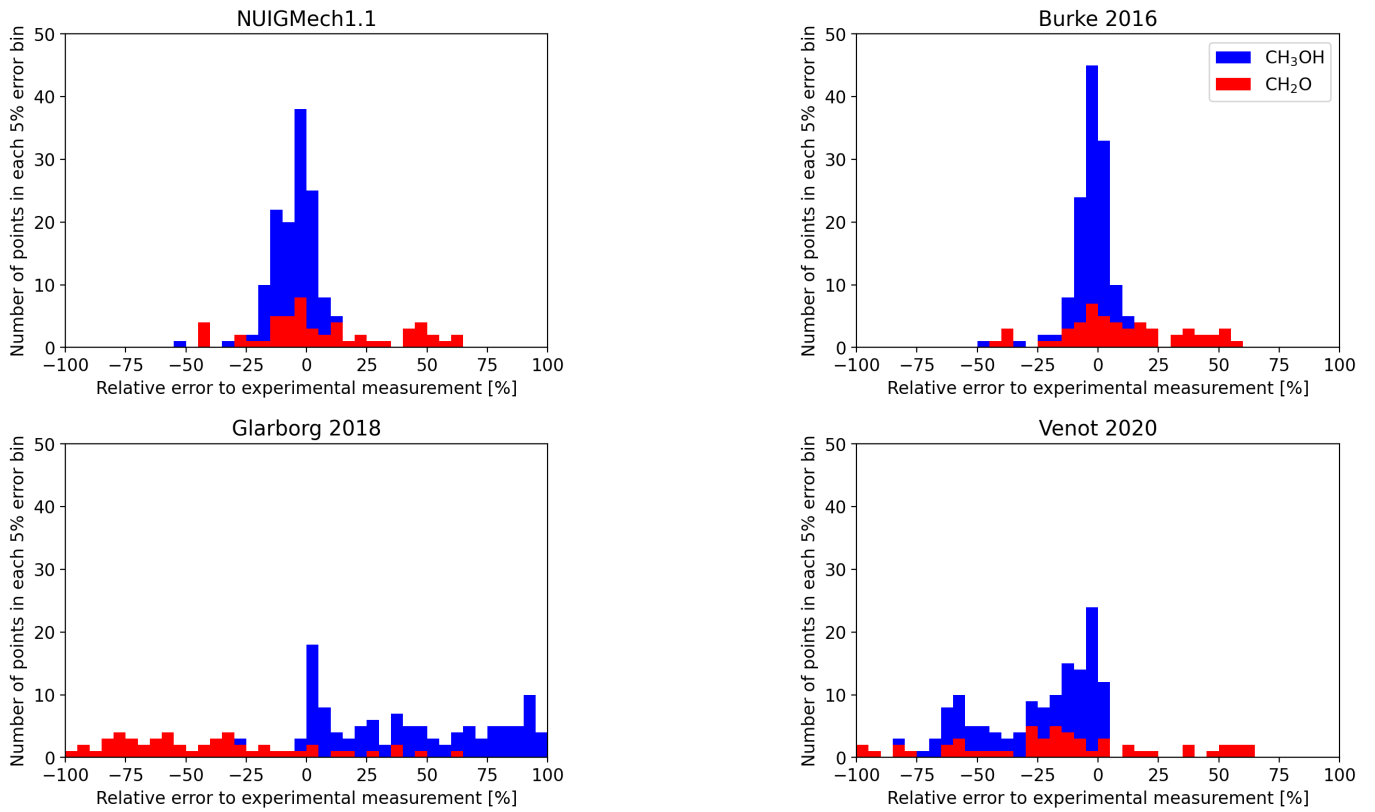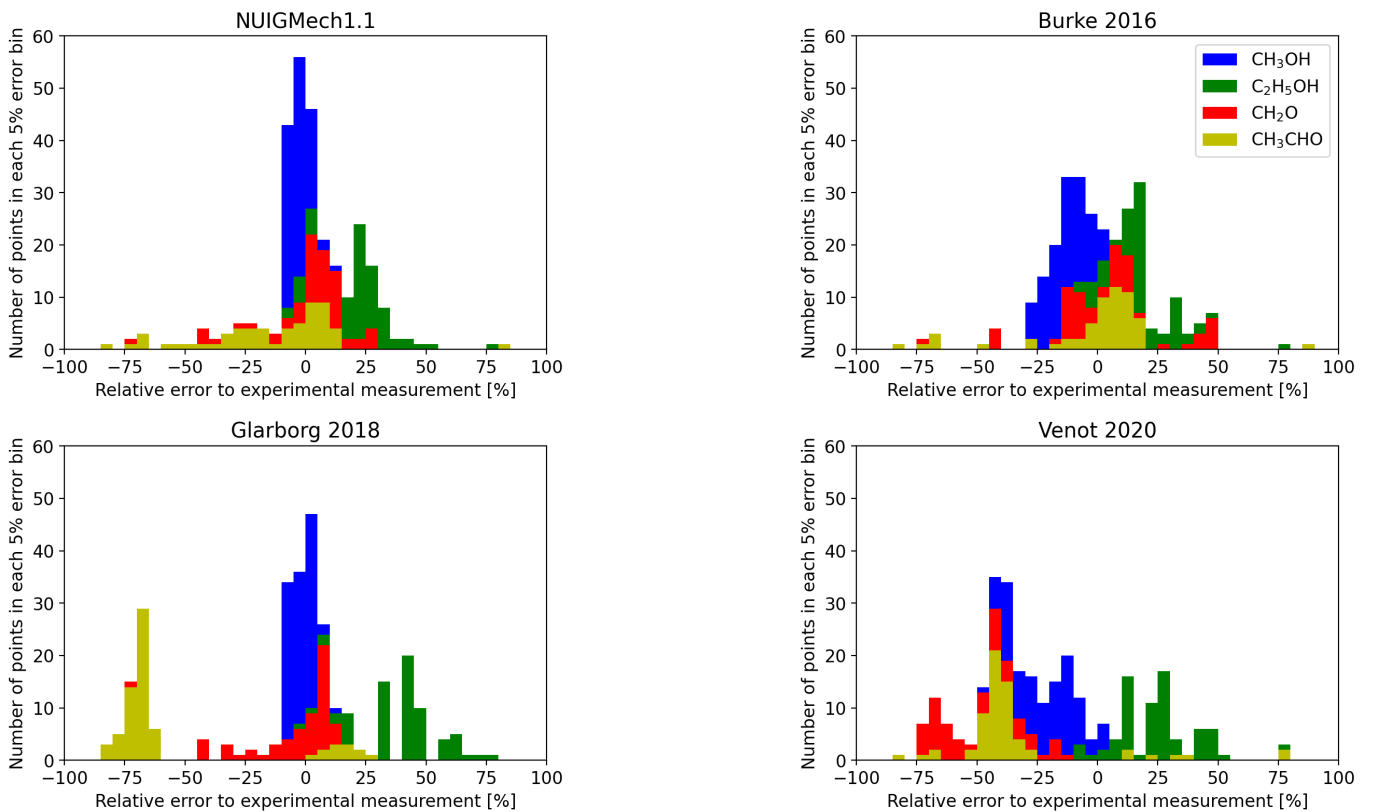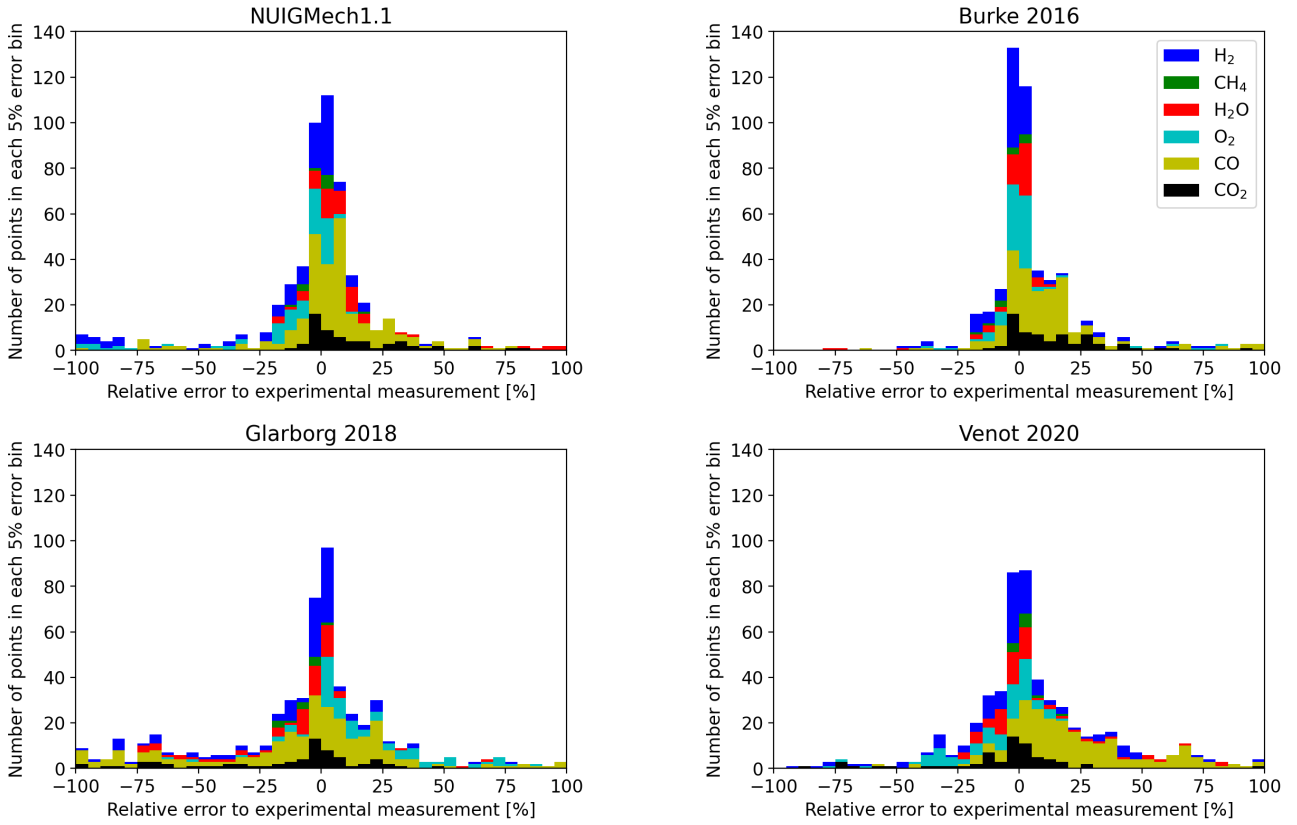## Appendix C: Statistical distributions of network errors

Fig. C.1. Statistical distribution of the relative error over the 155 experimental data points corresponding to combustion conditions of Fig. 3. Each color gathers all molar fraction measurements of the corresponding species.

Fig. C.2. Statistical distribution of the relative error over the 294 experimental data points corresponding to pyrolysis conditions of Fig. 3. Each color gathers all molar fraction measurements of the corresponding species.

Fig. C.3. Statistical distribution of the relative error over the 571 experimental data points corresponding to combustion conditions of Fig. 4. Each color gathers all molar fraction measurements of the corresponding species.
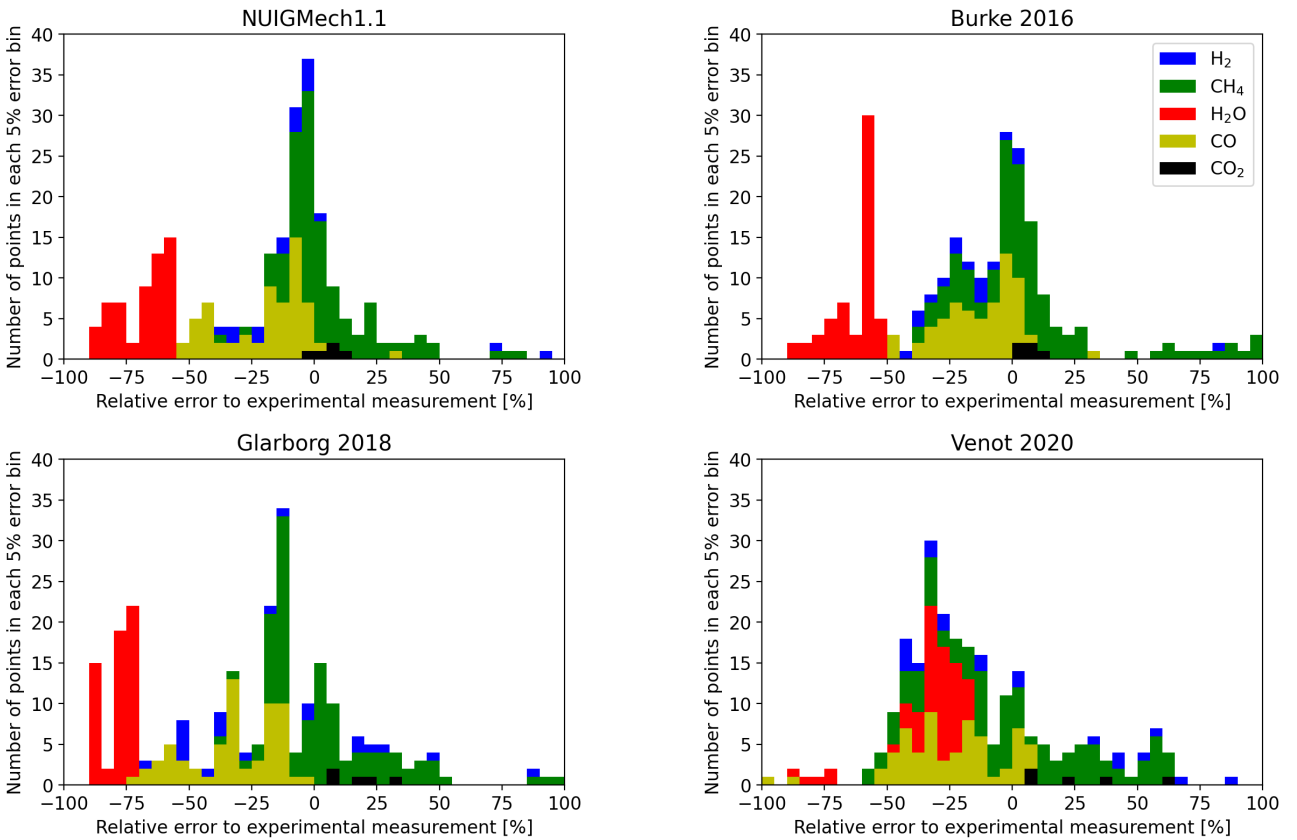

Fig. C.4. Statistical distribution of the relative error over the 252 experimental data points corresponding to pyrolysis conditions of Fig. 4. Each color gathers all molar fraction measurements of the corresponding species.

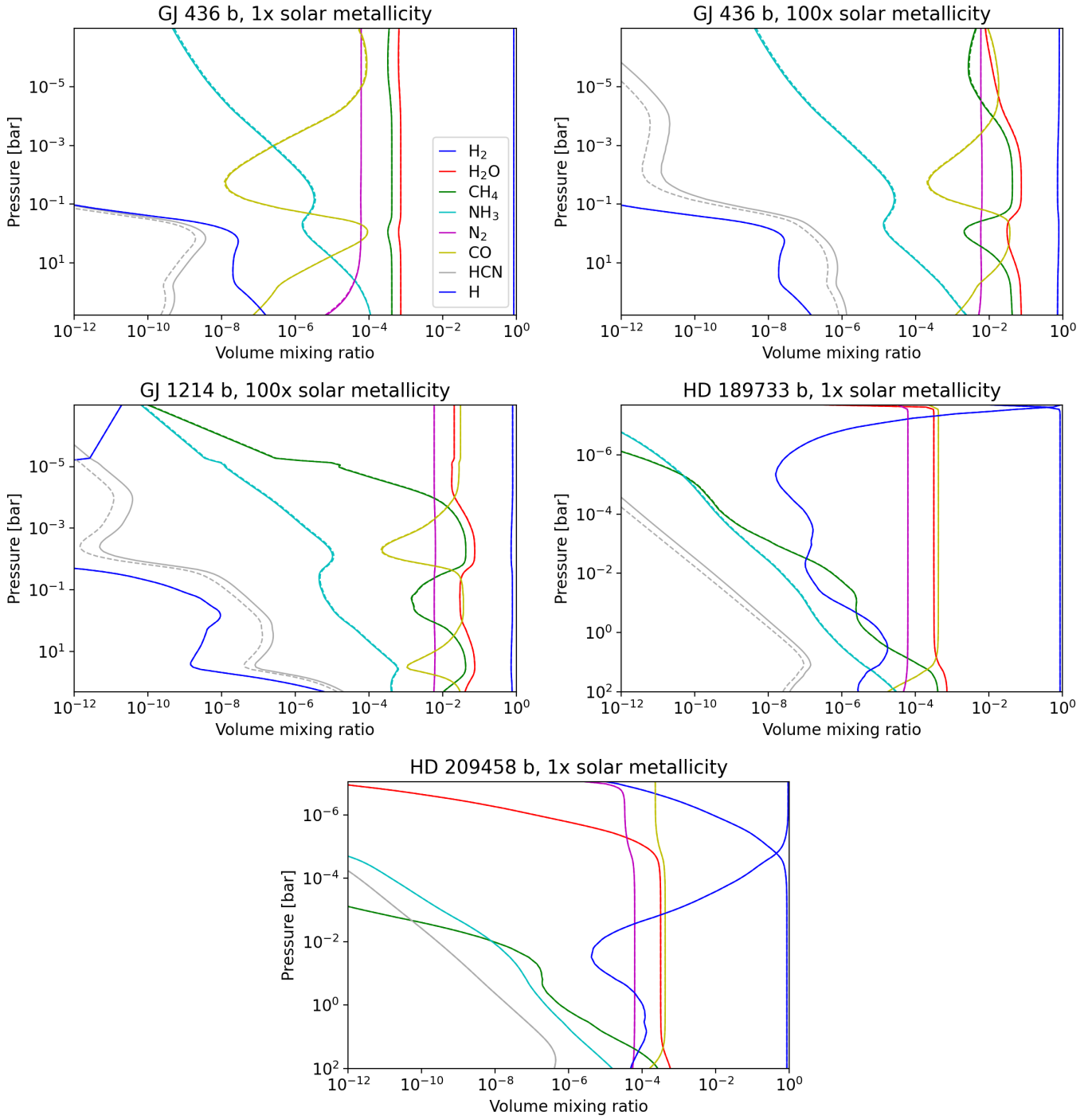# Appendix D: Thermochemical data

Fig. D.1. Thermodynamic equilibrium abundance profiles of the main species for all exoplanets cases in Table 3. Dashed lines are computed with the V20 thermodynamic data and solid lines are based on V23 thermodynamic data. In the last panel, all these lines overlap perfectly, indicating no difference for this PT profile.
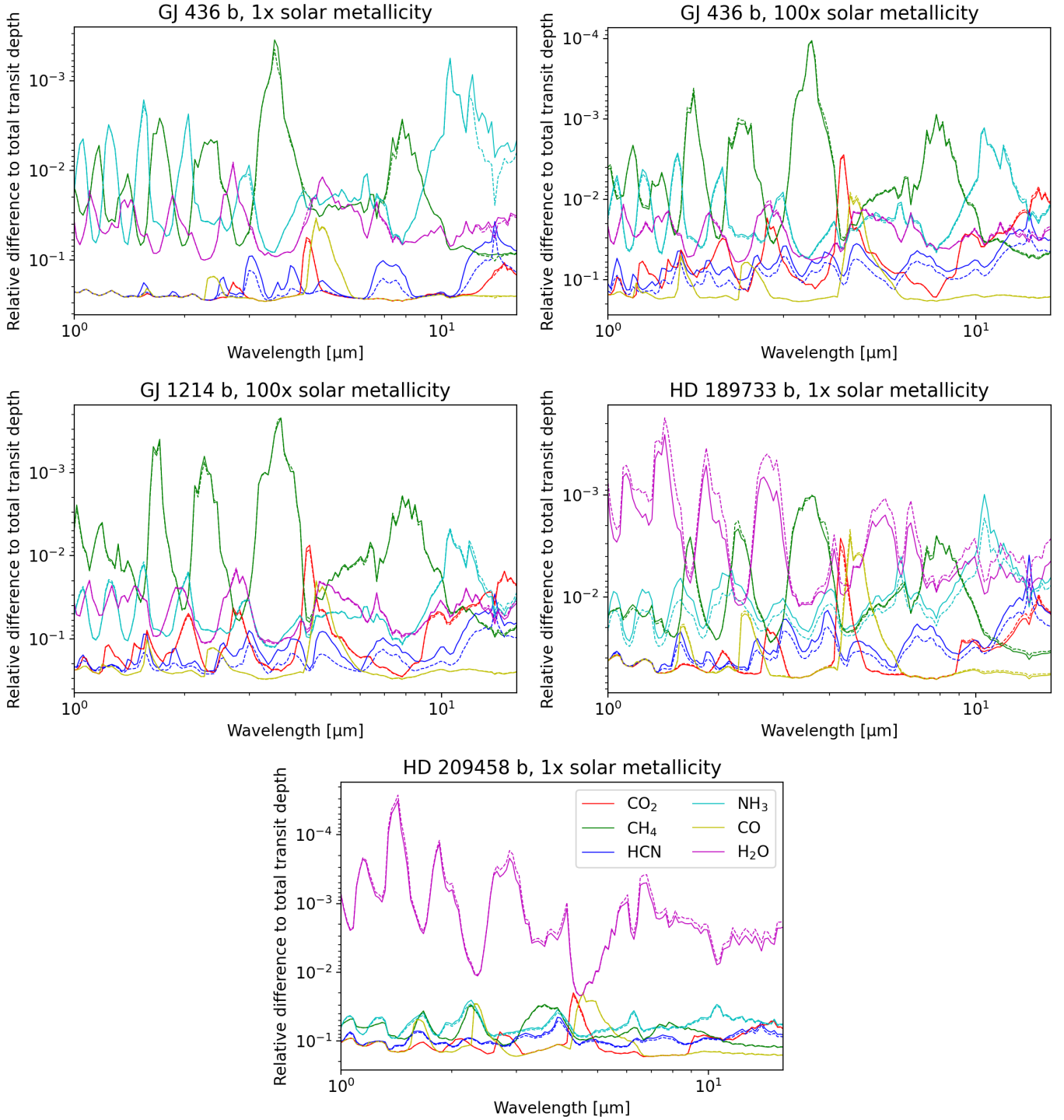
Appendix E: Transmission spectrum contributions

Fig. E.1. Contribution to the synthetic transmission spectra for all considered absorbing species. Dashed lines are computed from abundances obtained with V20, and solid lines from abundances obtained with V23. The plotted quantity is the relative difference to the total transit depth, $\frac{D_{tot} - D_{spec}}{D_{tot}}$, with D_{tot} being the total transit depth and D_{spec} being the contribution of the species to the total transit depth. For each wavelength, only the uppermost and close lines have significant impact on the spectrum.